Volume 1
Number 1
January 2022

Energy
Advances

rsc.li/energy-advances

ISSN 2753-1457

ROYAL SOCIETY
OF CHEMISTRY

ROYAL SOCIETY
OF CHEMISTRY

rsc.li/energy-advances

1

2

3

4

5

Recent Advances in Lanthanide-based Metal-Organic Frameworks for

6

Photocatalytic Hydrogen Evolution Application

7

P Danita Patricia[1] and Rajadurai Vijay Solomon[2]*

8

[1]MCC-MRF Innovation Park, Madras Christian College (Autonomous), East Tambaram,

9

Chennai – 600 059, Tamil Nadu, India.

10

[2]Department of Chemistry, Madras Christian College (Autonomous), East Tambaram,

11

Chennai – 600 059, Tamil Nadu, India.

12

email id: vjsolo@mcc.edu.in & vjsolo@gmail.com

13

14

15

16

17

18

19

20

21

Energy Advances Accepted Manuscript

Energy Advances Accepted Manuscript

22   **ABSTRACT**

23   Hydrogen is increasingly recognized as a promising clean fuel, offering a sustainable

24   alternative to fossil fuels with water as its only combustion byproduct. Given several

25   hydrogen production methods, photocatalytic water splitting stands out due to its potential

26   for harnessing abundant solar energy to generate hydrogen. Among numerous

27   photocatalysts reported for water-splitting, metal-organic frameworks (MOFs) exhibit

28   excellent photocatalytic activity due to their enormous surface area. In this field,

29   lanthanide-based MOFs (Ln-MOFs) have emerged as exceptional photocatalysts due to

30   their unique properties and customizable structures, enhancing light absorption and

31   charge separation. Recent advancements in the development of Ln-MOFs have

32   demonstrated their potential to achieve notable hydrogen evolution rates under solar

33   irradiation, positioning them at the forefront of renewable energy research. The

34   introduction of Ln-MOFs into photocatalytic water-splitting marks a new era with a

35   multitude of exciting possibilities ahead. In this context, a comprehensive overview of the

36   trends and technologies involved in designing and understanding Ln-MOFs for water

37   splitting is essential to developing efficient catalysts with enhanced properties. Here, we

38   focus exclusively on the role of Ln-MOFs in photocatalytic water splitting, providing an in-

39   depth analysis of their photocatalytic performance and stability. This review systematically

40   classifies Ln-MOFs based on modifications in their frameworks, examining how these

41   changes influence their properties and overall efficiency in hydrogen production. The

42   review highlights the progress made in the field while addressing the gaps in current

43   knowledge, particularly in understanding the mechanisms that govern the performance of

44   Ln-MOFs. Moreover, it outlines future directions for enhancing the efficiency and stability

45   of Ln-MOFs in hydrogen production, offering valuable insights that could guide further

46   research. In summary, this review will aid the naïve and young researchers in the MOF

47   domain to gain comprehensive knowledge on the nuances of lanthanide-based Ln-MOFs

48   and appreciate their significant role in developing new technology for H_2 production.

49   **Keywords:** Hydrogen production, Lanthanide-based metal-organic frameworks,

50   Photocatalytic water-splitting, Sustainable energy, Solar energy, Hydrogen Evolution

51   Reaction.

52   **LIST OF ABBREVIATIONS**

53   **AA** – Ascorbic Acid

54   **Ag** – Silver

55   **Al** – Aluminium

56   **AQE** – Apparent Quantum Efficiency

57   **ATA** – 2-aminoterephthalate

58   **Au** – Gold

59   **$BiVO_4$** – Bismuth Vanadate(V)

60   **BPDC** – Biphenyl-4,4′-dicarboxylic acid

61   **Bpy** – 2,2'-Bipyridine

62   **BPYDC** – 2,2′-Bipyridine-4,4′-dicarboxylate

63   **BTC** – Benzene-1,3,5-tricarboxylic acid

64   **CB** – Conduction Band

65   **CdS** – Cadmium(II) Sulfide

66   **Ce** – Cerium

67   **CeO$_2$** – Cerium(IV) Oxide

68   **CH$_3$NH$_3$PbI$_3$** – Methylammonium Lead Iodide

69   **CoPi** – Cobalt Phosphate

70   **COF** – Covalent Organic Framework

71   **CPP** – Conjugated Porous Polymer

72   **CSUST** – Changsha University of Science and Technology

73   **Cu** – Copper

74   **Cu$_2$O** – Copper(I) Oxide

75   **CZS** – Cadmium Zinc Sulfide

76   **DyCl$_3$·6H$_2$O** – Dysprosium(III) chloride

77   **Eu** – Europium

78   **Fe$_2$O$_3$** – Iron(III) Oxide

79   **Gd** – Gadolinium

80   **g-C$_3$N$_4$** – Graphitic Carbon Nitride

81   **H$_3$TCA** – Taurocholic Acid

82   **H$_4$abtc** – 3,3′,5,5′-azobenzene-tetracarboxylic acid

83   **H$_4$TPTC** – [1,1′:4′,1″]Terphenyl-3,3″,5,5″-tetracarboxylic acid

84   **Hcptpy** – 4'-(4-carboxyphenyl)-2,2':6',2"-terpyridine

85   **HER** – Hydrogen Evolution Reaction

86   **HOMO** – Highest Occupied Molecular Orbital

87   **La** – Lanthanum

88   **Ln** – Lanthanide

89   **Ln-MOF** – Lanthanide-Metal Organic Frameworks

90   **LMCT** – Ligand to Metal Charge Transfer

91   **LSPR** – Localized Surface Plasmon Resonance

92   **LUMO** – Lowest Unoccupied Molecular Orbital

93   **MIL** – Materials of Institute Lavoisier

94   **MOL** – Metal Organic Layer

95   **MoS$_2$** – Molybdenum(IV) Sulfide

96   **Na$_2$S** – Sodium Sulfide

97   **Na$_2$SO$_3$** – Sodium Sulfite

98   **NH$_4$F** – Ammonium Fluoride

99   **Ni** – Nickel

100   **OER** – Oxygen Evolution Reaction

101   **PHE** – Photocatalytic Hydrogen Evolution

102   **Pr** – Praseodymium

103   **PS** – Photosensitizer

104   **Pt** – Platinum

105   **RE-MOF** – Rare Earth Metal Organic Frameworks

106   **RuO$_x$** – Ruthenium Oxide

107   **SBU** – Secondary Building Unit

108   **SD** – Sacrificial Donor

109   **Tb** – Terbium

110   **TBAPy** – 4,4',4''-(Pyridine-2,4,6-triyl)tribenzaldehyde

111   **TEOA** – Triethanolamine

112   **TiO$_2$** – Titanium(IV) Oxide

Energy Advances Accepted Manuscript

113   **Tm –** Thulium

114   **VB** – Valence Band

115   **WO$_3$** – Tungsten(VI) Oxide

116   **Yb** – Ytterbium

117   **ZIS** – Zinc Indium Sulfide

118   **ZnO** – Zinc(II) Oxide

119   **1. INTRODUCTION**

120   The use of fossil fuels as conventional energy sources leads to greenhouse gas emissions,

121   significantly impacting climate patterns (1). With increasing concerns over climate change,

122   hydrogen is recognized as a cleaner, sustainable alternative. Its clean combustion, high

123   specific energy, storability, and generation of water as a byproduct make it an attractive

124   replacement for traditional fuels (2–6). Hydrogen is widely used in gas turbines (7),

125   aviation (6), automotive fuel (8,9), petroleum hydroprocessing (10), and fuel cells (11). To

126   meet growing hydrogen demand sustainably, efficient production methods are critical.

127   Hydrogen can be produced via steam methane reforming and methane pyrolysis from

128   natural gas, producing CO_2 and carbon (soot), respectively (Fig. 1) (12,13). Coal gasification

129   generates hydrogen with CO_2 as a by-product, contributing to the carbon footprint (14).

130   Alternatively, hydrogen is produced by anaerobic bacteria in artificial ecosystems under

131   dark conditions, where complex sugars break down into organic acids and hydrogen,

132   though the setup is costly and inefficient (15). Thermal decomposition of ammonia or

133   hydrocarbons can also generate hydrogen, with ammonia being CO_2-free but reliant on

134   non-renewable sources, while hydrocarbons produce carbon by-products (16,17). The

135 most straightforward method of all is to produce hydrogen through water-splitting. This

136 energy-driven process splits water molecules into oxygen and hydrogen with the help of a

137 catalyst (18–22).

138

139

140

141

142

143

144
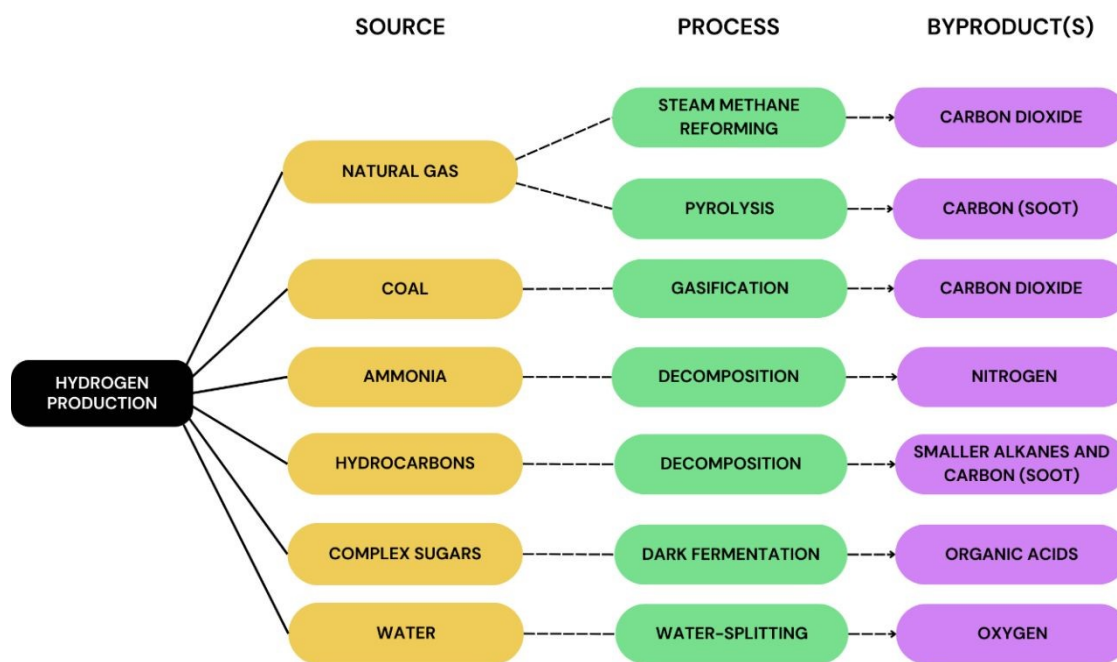
145 **Fig 1.** Sources, processes and byproducts of several hydrogen production methods.

146 Water-splitting is an environmentally benign method for hydrogen production, offering

147 zero carbon emissions and high efficiency (up to 80%) (23). Its only by-product is oxygen,

148 which has no adverse environmental impact, and the water source is abundant. This

149 sustainable process can be driven by thermal, biochemical, photonic, or electrical energy

150 (Fig. 2) (20,24). Thermal water splitting occurs at temperatures above 2500 K, but it faces

151 challenges such as complex reaction kinetics and the need for cooling material recovery

152 (19). Biochemical water splitting, involving cyanobacteria and algae in direct photolysis, is

153 greener but hindered by low efficiency, high costs, and large operational areas (18).

154
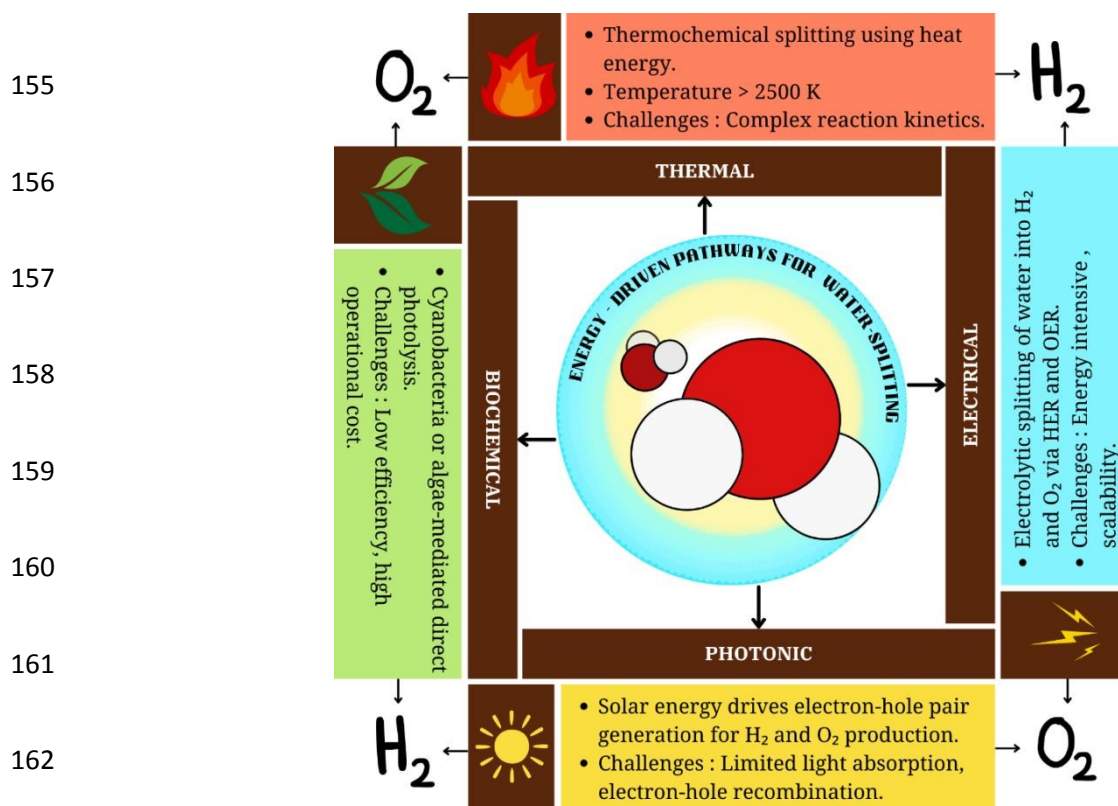
Fig 2. Various energy-driven pathways through which water can be split into its constituents.

Electrolysis is another widely known method, where water is split into hydrogen and oxygen by electricity. Hydrogen evolves at the cathode via the Hydrogen Evolution Reaction (HER), and oxygen at the anode via the Oxygen Evolution Reaction (OER) (25,26). However, this method requires high energy input and struggles with scalability (24). To overcome these limitations, photocatalytic water-splitting has emerged as an alternative. This process uses solar energy (photons) and a catalyst to generate electrons and holes that split water into hydrogen and oxygen. Photocatalytic water-splitting, or photocatalytic hydrogen evolution (PHE), is highly efficient, as a significant portion of solar photons can be utilized in the presence of an effective catalyst (24). This approach minimizes energy

174   conversion losses and represents a promising path toward sustainable hydrogen

175   production.

2. FUNDAMENTALS OF PHE

177   PHE involves four steps: (i) photon absorption, (ii) electron-hole pair generation, (iii)

178   carrier separation and migration, and (iv) surface reactions producing H_2 and O_2 (Fig. 3).

179   The process relies on photocatalysts, photosensitizers (PSs), and sacrificial donors (SDs).

180

181

182

183

184

185

186

187
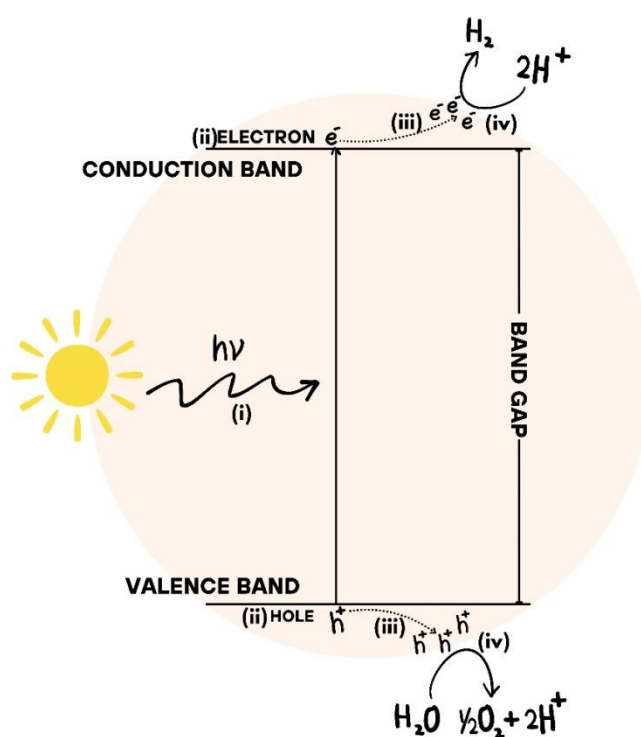
188   **Fig 3.** Key steps involved in the photocatalytic water-splitting process: (i) Photon

189   absorption; (ii) Electron-hole generation; (iii) carrier separation and migration; (iv) redox

190   reactions at the surface.

191   Upon light irradiation, electrons (e^-) in the photocatalyst's valence band (VB) are excited to

192   the conduction band (CB), leaving holes (h^+) behind (I). Holes oxidize water, generating

193 protons (II), which are reduced by CB electrons (III), forming H_2 and O_2. The overall

194 reaction is summarized below (IV) (27–29).

195 On irradiation, $\qquad 2h\nu \rightarrow 2e^- + 2h^+ \qquad$ (I)

196 Oxidation, $\qquad 2h^+ + H_2O_{(l)} \rightarrow 1/2\ O_{2\ (g)} + 2H^+ \qquad$ (II)

197 Reduction, $\qquad 2H^+ + 2e^- \rightarrow H_{2\ (g)} \qquad$ (III)

198 Overall reaction, $\qquad 2h\nu + H_2O_{(l)} \rightarrow\ 1/2\ O_{2\ (g)} + H_{2\ (g)} \qquad$ (IV)
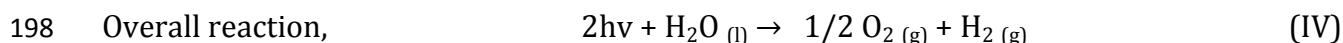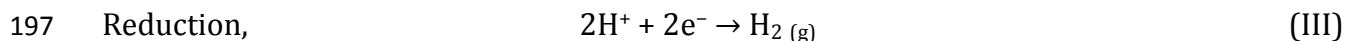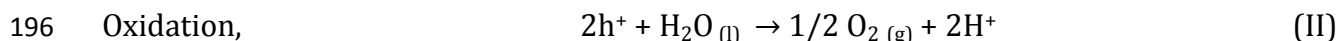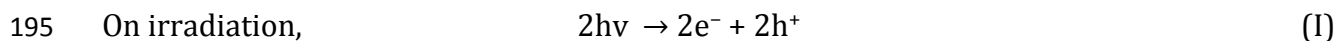
199 Photocatalysts enhance reaction rates by improving photogenerated carrier separation and

200 enabling broad-spectrum light absorption, providing more photons for the reaction. When

201 light energy exceeds the band gap, electron-hole pairs form. For water splitting, the CB

202 must be more negative than the H^+ reduction potential and the VB more positive than

203 water oxidation (29). Though water splitting requires 1.23 eV, practical applications need a

204 band gap of 1.6–2.2 eV (30). Smaller band gaps enable wider light absorption, while

205 crystallinity, particle size, and structure affect charge separation. Higher crystallinity

206 reduces defects, improving charge mobility and minimizing recombination, whereas

207 nanometer-sized particles enhance charge transfer but may increase recombination if too

208 small. Cocatalysts are essential for enhancing the performance of semiconductor

209 photocatalysts in H_2 evolution. Plasmonic metals like Au and Cu improve visible light

210 absorption through localized surface plasmon resonance (LSPR) effects (31,32). By

211 attracting electrons, cocatalysts facilitate efficient separation of electron-hole pairs and

212 enhance charge carrier transfer when integrated with photocatalyst surfaces (33,34).

213 Additionally, they provide active sites for photocatalytic reactions, functioning as electron

214 sinks and proton reduction sites (35,36). Cocatalysts also improve the stability of

215 photocatalysts, particularly metal sulfides, by extracting photogenerated holes, thereby

216 preventing self-decomposition and supporting oxygen evolution reactions, ultimately

217 boosting overall photocatalytic efficiency (37,38).

218   PSs harvest sunlight and initiate redox reactions for solar fuel generation by absorbing

219 photons and exciting an electron to form PS*. PS* undergoes reductive or oxidative

220 quenching and is regenerated in catalytic reactions, producing solar fuels like hydrogen or

221 reducing CO_2. Efficient PSs require long excited state lifetimes for electron transfer and

222 should absorb a broad light spectrum, especially visible light, to optimize sunlight

223 utilization (39–43). SDs are essential in artificial photosynthesis, particularly for water

224 splitting. Acting as electron sources, they sustain electron flow, prevent reverse reactions

225 with oxidized products like oxygen, and ensure continuous hydrogen production. Effective

226 systems require compatible redox potentials between PSs and SDs, accounting for the PS's

227 excited state lifetime and catalytic needs. SDs are irreversibly oxidized, enabling PS

228 operation but generating chemical waste and requiring replenishment, which reduces

229 sustainability (44–47). PSs also face photobleaching and back electron transfer, causing side

230 reactions and lower efficiency (43). Research aims to develop photocatalysts that drive

231 water splitting independently, eliminating reliance on SDs and PSs, thus improving

232 efficiency and sustainability.

233 In recent decades, numerous photocatalysts have been explored for water splitting. TiO_2,

234 studied since the 1970s, remains a key material due to its abundance, stability, and

235 favorable band alignments. However, its wide band gap (3.2 eV) limits light absorption to

236 the UV region, and issues with conductivity and recombination persist (48). Improvements

237   include band gap modification, nanostructuring, defect control, co-catalyst decoration, and

238   heterojunctions. Other materials like Fe_2O_3, WO_3, ZnO, $BiVO_4$, Cu_2O, and CdS offer narrower

239   band gaps (2.0–2.5 eV) but face challenges such as low carrier mobility and

240   crystallographic disorder (49–58). Emerging materials, including graphene-based materials,

241   perovskites (e.g., $CH_3NH_3PbI_3$, $CsPbBr_3$), and 2D materials (e.g., MoS_2, g-C_3N_4), show

242   promise due to their unique properties. However, they face issues with light absorption,

243   stability, scalability, toxicity, and synthesis (59–63). In addition, covalent organic

244   frameworks (COFs), conjugated porous polymers (CPPs), and porphyrins are promising

245   photocatalysts for water splitting due to their distinct features. COFs offer tunable band

246   gaps, high porosity, and extended π-conjugation for efficient charge separation and light

247   absorption (64,65). CPPs exhibit broad visible-light absorption and delocalized π-electrons,

248   enhancing charge transport (66,67). Porphyrins serve as efficient light-harvesters and

249   electron transfer agents, functioning as both photosensitizers and catalytic sites (68–70).

250   However, metal-organic frameworks (MOFs) surpass these materials with abundant

251   catalytic sites, exceptional structural tunability, and superior photocatalytic performance

252   due to the presence of metal centers, positioning them as frontrunners in water-splitting

253   applications.

254   MOFs are crystalline structures formed by coordinating organic linkers with metal ions or

255   clusters that offer high porosity and versatility. Constructed from metals like transition

256   metals, lanthanides, and actinides, mixed-metallic MOFs incorporate multiple metals (71).

257   Organic linkers, including carboxylate, azolate, phosphonate, sulfonate, and pyridyl groups,

258   enable diverse structures from 1D chains to 3D networks (72,73). Some representative

259   examples of linkers from each class have been depicted in Fig. 4. The general classification

260 of MOFs based on porosity, dimensionality, type of node, type of linker, and topology is

261 depicted in Table 1. Certain MOFs have rigid frameworks, ideal for harsh environments,

262 while flexible ones enable reversible gas adsorption (74). High-valent metals and rigid

263 linkers enhance thermal stability, making MOFs adaptable for addressing limitations in

264 conventional materials.
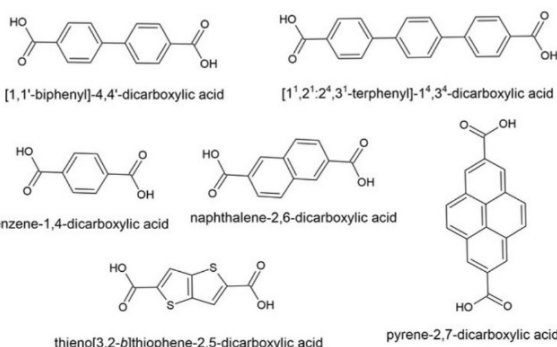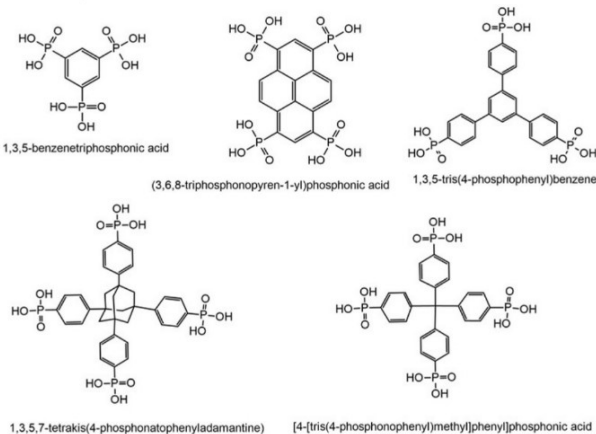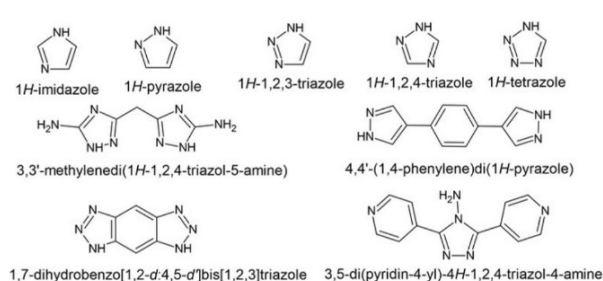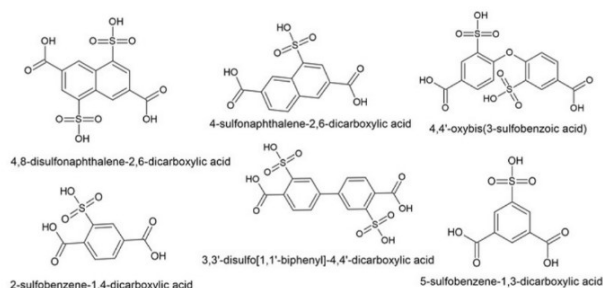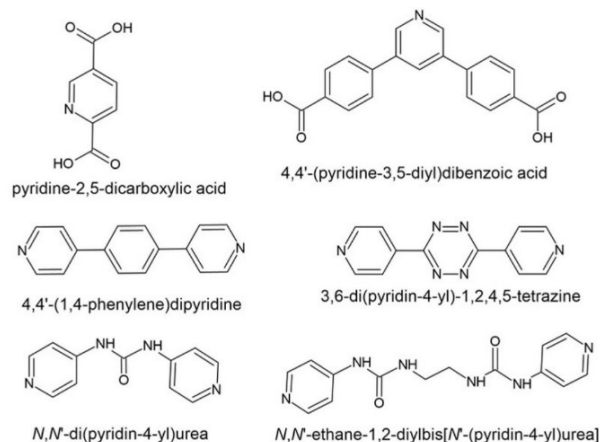
Fig 4: Some representative examples of ligands (a)Carboxylate (b)Phosphonate (c)Azolate (d)Sulphonate and (e)Pyridyl.

CLASSIFICATION	TYPES	EXAMPLES	REFERENCES
Dimensionality	1- Dimensional	IMP – 27Na	(75)
		MIL-132	(76)
		Mg-MOF-74	(77)
		CAU-50	(78)
	2 – Dimensional	ULMOF-1	(79)
		AgPb-MOF	(80)
		CTH-15	(81)
			(82)
		COK-47	
	3 - Dimensional	MOF – 808	(83)
		KGF-1	(84)
		CAUMOF-8	(85)
		CdNa-MOF-1	(86)
Porosity	Microporous (<2 nm)	ZIF-8	(87)
		MOF-508	(88)
		$[Zn(bdc)(ted)_{0.5}]\cdot 2\,DMF\cdot 0.2\,H_2O$	(89)
		$[Cu(INA)_2]$	(90)
	Mesoporous (2– 50 nm)	MIL-100(Cr)	(91)
		ZIF-100	(92)
		MOF-180	(93)
		NOTT-116(PCN-68)	(94)
	Carboxylate	FeNi-DOBDC	(95)
		CoNi-MOFNA	(96)

Type of organic linker	Azolate	ZIF-8	(97)
		ZIF-67	(98)
	Pyridyl	$\{[Cu^{I}I][Cu^{II}(pdc)(H_2O)]\cdot 1.5MeCN\cdot H_2O\}_n$	(99)
		67BPym-MeI	(100)
	Sulphonate	PAMPS@MIL-101-SO$_3$H	(101)
		UiO-66-SO$_3$H	(102)
	Phosphonate	IPCE-1Ni	(103)
		TUB75	(104)
Type of metal nodes	Single	MIL-53(Fe)	(105)
	Clusters	Uio – 66	(106)
		NH$_2$-MIL – 125	(107)
Topology	Simple	MOF-5	(108)
		HKUST-1	(109)
		ZTF-1	(110)
	Complex	PCN-222	(111)
		MOF-74	(112)

279

280 **Table 1.** General classification of MOFs based on dimensionality, porosity, type of organic

281 linkers, topology and type of metal nodes.

282 MOFs are renowned for high porosity, vast internal surface areas, and tunable pore sizes,

283 making them ideal for gas storage, separation, and catalysis (113,114). By varying linker

284 lengths, MOFs achieve selective gas capture, such as CO_2 from flue gas, and hydrocarbon

285 separation in petrochemical processes (72,115,116). Their modular synthesis enables

286 functional group introduction during or after synthesis, enhancing trapping and catalytic

287 performance (117–119). Many MOFs are biocompatible for drug delivery, while others

288 excel in heterogeneous catalysis due to large surface areas, tunable pores, and catalytic

289 active sites (72,120–123). Catalytic MOFs integrate metal ions or clusters or functionalized

290 linkers, with porosity allowing easy access to active sites (124). MOFs maintain structural

291 integrity after post-synthetic modifications, enhancing versatility (28).

292 As photocatalysts, MOFs absorb light and generate reactive species for pollutant

293 degradation and water-splitting. Their ability to absorb broad-spectrum light supports

294 electron-hole generation and efficient charge separation (125). The first MOF

295 photocatalyst, Al-ATA, consists of $AlO_4(OH)_2$ octahedral clusters linked by 2-

296 aminoterephthalates (ATA). Incorporating Ni(II) enabled Al-ATA to produce hydrogen at

297 36.0 µmol h^{-1}, establishing it as the first water-splitting photocatalyst (126). Another

298 breakthrough was MIL-125-CoPi-Pt, with cobalt phosphate (CoPi) and Pt cocatalysts, which

299 reached H_2 and O_2 production rates of 42.33 µmol h^{-1} and 21.33 µmol h^{-1}, suppressing

300 electron-hole recombination (127). In another instance, MIL-125-NH_2 with Pt and RuOx

301 cocatalysts enhanced H_2 and O_2 production to 85 µmol g^{-1} and 218 µmol g^{-1} over 24 h,

302 achieving 0.32% quantum efficiency (128). Introducing defects, such as plasma-treated Ti-

303 oxo clusters in MIL-125-NH_2, improved photocatalytic activity (129).

304 Despite advancements, transition metal MOFs often show low light response, necessitating

305 cocatalysts. Incorporating lanthanides into MOFs has emerged as a solution. Lanthanide-

306 based MOFs (Ln-MOFs) exhibit high coordination numbers, well-defined energy levels,

307 luminescence, and catalytic properties (130–132). Combining lanthanide properties with

308 MOFs opens opportunities for tailored photocatalytic water splitting (133,134). This

309 review explores Ln-MOFs in photocatalytic water splitting, discussing their structural

310 diversity, optical properties, and catalytic efficiencies.

311 3. SCOPE OF THE REVIEW

312 Since 2017, when An et al. first introduced the concept of MOFs as photocatalysts for

313 hydrogen production via water-splitting, the field has seen a surge in research activity

314 (126). Numerous studies have since explored the potential of MOFs and their derivatives in

315 this domain, highlighting their unique structural advantages and catalytic capabilities. The

316 ongoing interest in MOF-based photocatalysis has led to the publication of several

317 comprehensive reviews, each summarizing the latest advancements and providing insights

318 into various aspects of this technology (Table 2) (135–148). Reddy et al. provide a

319 comprehensive analysis of MOF-based heterogeneous photocatalysts, highlighting

320 applications in hydrogen generation, CO_2 reduction, and organic dye photodegradation

321 (135). On the other hand, Liu et al. have focused on the photocatalytic hydrogen production

322 applications of MOF-based materials across the UV, visible, and near-IR regions (136). Luo

323 et al. classify MOF-based and MOF-derived photocatalysts, elucidating how modifications

324 enhance photocatalytic performance (137). Nguyen's review identifies key achievements

325 and limitations in MOF photocatalysts for water splitting, suggesting future research

326   directions (138). Xiao et al. emphasize MOF-based heterostructures for hydrogen

327   production, particularly the factors affecting interfacial charge transfer (139). Nordin et al.

328   review synthetic methods, surface functionalization, elemental doping, ligand modification,

329   and heterojunction techniques to improve MOF photocatalytic properties (142). Sun et al.

330   discuss advances in photocatalytic water splitting and CO_2 reduction using MOF-based

331   materials, emphasizing structural features influencing catalytic activity (141). Despite

332   extensive research on MOFs, the photocatalytic water-splitting applications of lanthanide-

333   based MOFs (Ln-MOFs) remain underexplored. Most reviews focus on broader catalytic

334   applications of rare earth (RE) MOFs. For instance, Sun et al. summarize RE-MOFs for

335   organic reactions, photocatalysis, and CO oxidation but do not address Ln-MOFs in water

336   splitting (140). Saraci et al. classify RE-MOFs by metal composition, discussing sensing,

337   imaging, and catalysis without emphasis on water splitting (143). Similarly, Shi et al.

338   review RE-MOFs in energy conversion but provide limited insights into their photocatalytic

339   water-splitting potential (144).

340   Fan et al. explore RE-modified MOFs for photo/electrocatalysis, emphasizing RE elements'

341   theoretical advantages in MOF modification but lacking specific discussion on Ln-MOFs for

342   water splitting (145). Meng et al. address photocatalytic and electrocatalytic applications of

343   RE-MOFs, including hydrogen evolution and CO_2 reduction, but again do not focus on Ln-

344   MOFs in water splitting (146). Zhang et al. review RE-MOF synthesis and photon-related

345   applications, including fluorescence detection and luminescence, emphasizing Ce, Eu, Tb,

346   Yb, and Gd but only briefly addressing water splitting (147). Zhang et al. also summarize

347   Ln-MOFs' catalytic applications, including photocatalysis, but further exploration of their

348   role in water splitting is warranted (148). This review is one of the few that specifically

349   addresses the role of lanthanides in MOF-based catalysis, but it still leaves room for a more

350   detailed exploration of their use in water splitting. Here is a table summarizing the pros

351   and cons of the previously existing reviews, along with the strengths of the current

352   manuscript:

Review	Pros	Cons	Strengths of this review
Reddy et al. (135)	Comprehensive analysis of MOF-based heterogeneous photocatalysts for various applications, including H_2 generation.	Limited focus on Ln-MOFs and photocatalytic water splitting.	Dedicated focus on Ln-MOFs for hydrogen production, filling the gap in prior studies.
Liu et al. (136)	Explores photocatalytic hydrogen production across UV, visible, and near-IR regions.	Does not specifically highlight Ln-MOFs or modifications enhancing PHE performance.	Provides a detailed exploration of Ln-MOFs' unique properties for enhanced photocatalysis.
Luo et al. (137)	Framework for understanding how MOF modifications enhance photocatalytic performance.	General MOF focus with limited mention of Ln-MOF-specific applications.	Offers specific insights into Ln-MOF modifications and their effects on water splitting.
Nguyen et al. (138)	Identifies key achievements and limitations in MOF photocatalysts for water splitting.	Does not detail the unique role of lanthanides in MOF-based water-splitting photocatalysis.	Highlights the distinctive advantages of lanthanide metals in water-splitting applications.
Xiao et al. (139)	Emphasis on heterostructures and interfacial charge transfer for enhanced	Neglects lanthanide-specific systems and applications in	Provides an in-depth analysis of Ln-MOF-based heterostructures for

	photocatalysis.	photocatalytic water splitting.	PHE performance.
Nordin et al. (139)	Extensive overview of synthetic methods and functionalization techniques for MOFs.	Limited discussion on lanthanides and their specific photocatalytic capabilities.	Explores Ln-MOF-specific synthesis and functionalization for optimal PHE performance.
Sun et al. (141)	Highlights advances in water splitting and CO_2 reduction using MOF-based materials.	Minimal focus on lanthanide-based systems and their unique contributions.	Offers a comprehensive review of Ln-MOFs specifically for hydrogen production.
Zhang et al. (148)	Detailed synthesis methods and applications of RE-MOFs in various fields.	Lacks a focused discussion on Ln-MOFs as catalysts in PHE .	Exclusively examines Ln-MOFs for PHE.
Shi et al. (144), **Fan et al.** (145) , **Meng et al** (146).	Highlights general RE-MOF applications in energy and environmental catalysis.	Limited insights into lanthanide-specific photocatalytic water-splitting capabilities.	Bridges the gap by providing detailed analysis of Ln-MOFs in water-splitting technologies.

353

354 **Table 2** : Pros and cons of the previously existing reviews, and the strengths of the current review.

355   Given the limited focus on lanthanide-based MOFs in the existing literature, there is a clear

356   need for a dedicated review that comprehensively examines their applications in

357   photocatalytic water splitting. Such a review would not only fill a significant gap in the

358   current body of knowledge but also provide valuable guidance for future research in this

359   promising area. Therefore, this review aims to exclusively discuss the application of

360   various Ln-MOFs and their derivatives for hydrogen production through the PHE process,

361   offering a detailed analysis of the latest advancements in the past 10 years and highlighting

362   potential areas for further exploration. Relevant articles were gathered using the Google

363   Scholar search engine. Additionally, special issues focusing on the catalytic applications of

364   MOF materials were instrumental in identifying related studies (149–151).

365   4. LANTHANIDE MOFs FOR PHE

366   When the catalytic properties of MOFs began to be understood in the early 2000s, Ln-MOFs

367   started to gain significant attention around the mid-2010s. These frameworks were

368   initially explored for their unique luminescent properties. In 2007, researchers such as

369   Chen et al. and Cheng et al. delved into the luminescent characteristics of lanthanide metal

370   nodes within the MOFs, investigating their potential applications in sensing technologies

371   (152,153). The journey into understanding MOFs deepened in 2012 when Ramya et al.

372   conducted studies on energy transfer within these metal nodes (154). They focused on the

373   energy transfer from a terbium (Tb^{3+}) center to a europium (Eu^{3+}) center in a mixed-

374   lanthanide MOF. This work set the stage for further exploration into the photophysical

375   properties of these materials. Subsequently, Lin and Zhang provided a comprehensive

376   overview of energy transfer processes and light-harvesting capabilities in Ln-MOFs,

377 highlighting their potential in various photonic applications (155). In 2019, a notable

378 breakthrough occurred with the report of a La-MOF for hydrogen generation. The material

379 was found to have a band gap of 3.1 eV. Through cyclic voltammetry, the LUMO energy was

380 determined to be -2.5 V, which is more negative than the reduction potential of hydrogen,

381 suggesting that the MOF could be effectively used to generate hydrogen, opening new

382 avenues for clean energy applications (156). Following this, in 2020, researchers studied the

383 effects of incorporating lanthanides into the nodes of UiO-66, a well-known MOF, on its

384 catalytic activity (157). This research provided valuable insights into the catalytic behavior

385 of Ln-MOFs, demonstrating the potential in various catalytic processes.

386 These light-harvesting properties of Ln-MOFs originate from the lanthanide metals present

387 in the MOFs. These lanthanides display special optical properties owing to the 4d electron

388 layer in the metals, thereby activating the framework under photoexcitation conditions.

389 Additionally, the 4f orbitals, shielded by the filled 5s and 5p subshells, create multiple low-

390 lying empty states in the 4f shell (130). These orbitals are responsible for the unique

391 electronic properties of lanthanides, leading to sharp emission lines and long-lived excited

392 states. These characteristics make lanthanides suitable candidates to strengthen the light-

393 harvesting nature of MOFs. Incorporation of lanthanides into MOFs can effectively modify

394 the bandgap and electronic structure of the material. Furthermore, Ln-MOFs exhibit high

395 photostability, ensuring structural integrity and catalytic activity for prolonged periods of

396 irradiation (158). Ln-MOFs hold great promise in the realm of PHE due to their permanent

397 porosity, impressive structural diversity, high coordination number, and the flexible

398 coordination environment of lanthanides (133,159). One of the key features of these MOFs

399 is their ability to incorporate functional organic ligands, support and convert into various

400 derivatives (160,161). The desirable qualities of Ln-MOFs, such as high surface area,

401 tunable pore size, and chemical and thermal stability, make them excellent candidates for

402 catalysts (148) . By leveraging the properties of lanthanides, Ln-MOFs can achieve efficient

403 charge separation and transfer, reduced recombination rates, and thereby increased

404 overall efficiency in photocatalytic water-splitting applications.
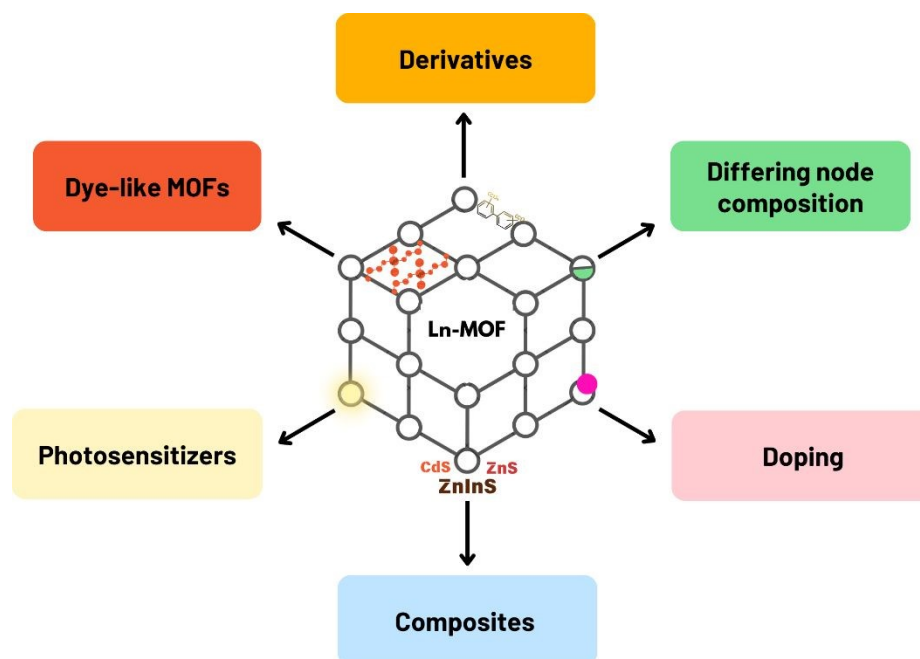
412 **Fig 5.** A graphical overview illustrating various Ln-MOF modifications.

413 This review aims to highlight the performance and stability of various Ln-MOFs in PHE

414 applications, drawing from case studies to illustrate their potential. The graphical overview

415 provided in Fig. 5 encapsulates the topics of discussion that follow.

416 **4.1. Differing node composition**

417 To enhance the photo-response of MOFs, one effective strategy is to incorporate a different

418 transition metal into the framework, aside from the one already constituting the Secondary

419 Building Units (SBUs). This subsection discusses the effect of the incorporation of various

420   lanthanide metals on a single MOF framework with the help of a few relevant studies. This

421   mixed-metal approach facilitates electron transfer from one metal to another, thereby

422   decreasing the band gap and increasing charge separation efficiency. In this context,

423   incorporation of Ce^{4+} into the framework is said to increase the efficiency of the catalyst,

424   due to the low-lying empty 4f orbitals of the lanthanide (162,163).

425   In 2020, a study by A. Melillo et al., examined the catalytic activities for overall water-

426   splitting for a series of five UiO-66 (M: Zr, Zr/Ti, Zr/Ce, Zr/Ce/Ti, Ce) materials. It was

427   found that the activity of the trimetallic MOF was seven times higher than its single metal

428   analogue that contained only Zr (157). The band gap of the trimetallic MOF was

429   determined to be 3.10 eV with the help of UV-DRS. This makes UiO-66 (Zr/Ce/Ti) a suitable

430   catalyst for water splitting, since at pH 7 the CB energy must be higher than -4.03 eV for the

431   evolution of H_2 from water. Among the five members, the catalytic activity for overall water

432   splitting followed the order UiO-66(Zr/Ce/Ti) > UiO-66(Zr/Ti) > UiO-66(Zr/Ce), whose

433   activities were higher than that of the single metal MOF, when irradiated with a xenon laser

434   in the presence of a cut-off filter (λ > 450 nm) (157). The quantum yields for the reactions

435   were found to be 0.55, 0.055, and 0.1 at 300 nm, 400 nm and 500 nm respectively,

436   indicating the highest relative efficiency at 300 nm. However, the maximum amount of

437   hydrogen was generated at 400 nm (Fig. 6a). Reusing the UiO-66(Zr/Ce/Ti) catalyst caused

438   a minor decrease in the initial rate of reaction as well as the final volume of hydrogen

439   produced (Fig. 6b). The use of a sacrificial donor, namely methanol, along with the MOF,

440   resulted in the increase of the amount of hydrogen production by two-fold, up to 390 μmol

441   g^{-1} in 22 hours. This is much higher than that of individual UiO-66 (~155 μmol g^{-1}) (157).
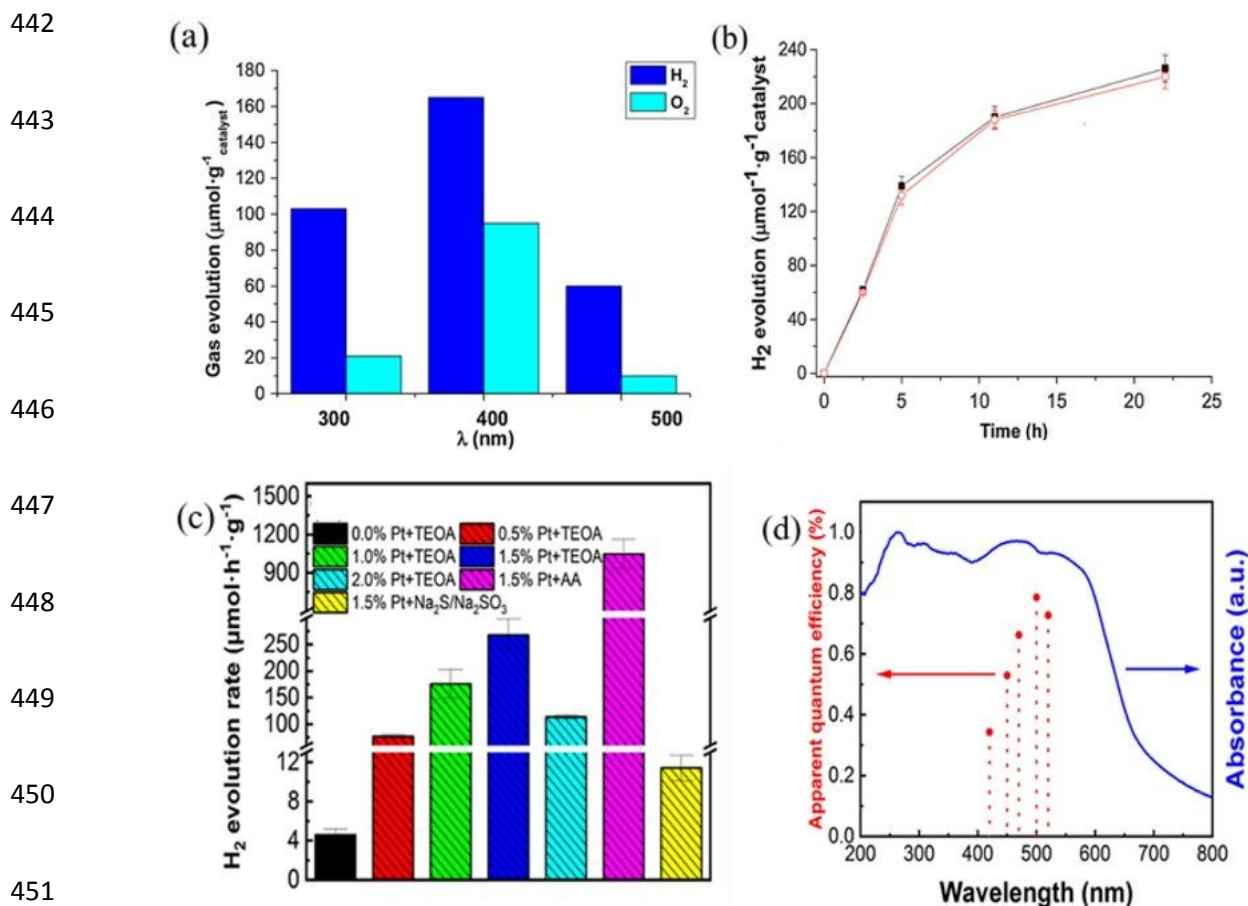
Fig 6. (a) Diffuse reflectance UV–vis spectra of a) UiO-66 (Zr), b) UiO-66 (Zr/Ti), c) UiO-66 (Zr/Ce), d) UiO-66 (Zr/Ce/Ti), e) UiO-66 (Ce). The inset (at right) corresponds to a magnification of the 400-650 nm region for plots a, b, c and d. (b) Photocatalytic H_2 evolution in the overall water splitting for two consecutive uses of UiO-66 (Zr/Ce/Ti): first use (▨); second use (○).Reprinted with permission from ref. (157). Copyright 2020 Elsevier (c) H_2 evolution rates of Pr-MOF-Ru(cptpy)$_2$ catalysts under different conditions (d) Wavelength dependence of the AQE of 0.5% Pt/Eu-MOF-Ru(cptpy)$_2$. Reprinted with permission from ref. (164). Copyright 2023 ACS

Cerium plays a multifaceted role in UiO-66 (Zr/Ce/Ti), enhancing photocatalytic activity through improved charge separation, increased light absorption, enhanced structural

462 stability, and synergistic interactions with other metals. The improved photocatalytic

463 efficiency of the MOF was attributed to kinetic factors like charge separation and

464 recombination rather than thermodynamic factors like band gap alignment (157)

465 Following this, in 2023, two MOFs, Eu-MOF-Ru(cptpy)$_2$ and Pr-MOF-Ru(cptpy)$_2$, were

466 synthesized using the ruthenium complex Ru(cptpy)$_2$ as the organic linker, with europium

467 (Eu(III)) and praseodymium (Pr(III)) ions serving as the metal nodes, respectively. To

468 enhance their catalytic performance, platinum (Pt) nanoparticles were photodeposited

469 onto the surfaces of the MOFs, acting as co-catalysts. The catalytic performance was

470 evaluated in a triethanolamine aqueous solution, which served as a sacrificial agent. For Pr-

471 MOF-Ru(cptpy)$_2$, an optimal H$_2$ evolution rate of 268 μmol g^{-1} h^{-1} was achieved with a

472 1.5% Pt loading. However, when ascorbic acid (AA) was used as a sacrificial reagent, the H$_2$

473 evolution rate significantly increased to 1047 μmol g^{-1} h^{-1} (Fig. 6c). This enhancement was

474 attributed to the better matching of AA's redox potential with the VB of the Pr-MOF,

475 facilitating more efficient electron transfer. In contrast, Eu-MOF-Ru(cptpy)$_2$ exhibited

476 superior photocatalytic performance with a lower Pt loading of 0.5%, achieving an

477 impressive H$_2$ evolution rate of 4373 μmol·h^{-1}·g^{-1} in the presence of ascorbic acid. The

478 apparent quantum efficiency (AQE) of this catalyst was measured at 0.79% at 500 nm,

479 indicating its excellent ability to absorb and utilize visible light for photocatalysis (Fig. 6d)

480 (164).

481 The Eu-MOF catalyst also demonstrated remarkable stability; it maintained its catalytic

482 activity over 9 hours of continuous reaction, showing little to no degradation (Fig. 7a). In

483 contrast, the Pr-MOF catalyst exhibited a significant decrease in activity over the same

484 period, likely due to instability in the ascorbic acid solution, which led to the decomposition

485 of the MOF structure (Fig.7c). These findings highlight the potential of Eu-MOF-Ru(cptpy)$_2$

486 as a highly efficient and stable photocatalyst for hydrogen production under visible light,

487 with a lower requirement for Pt loading and better performance compared to Pr-MOF-

488 Ru(cptpy)$_2$ (164).
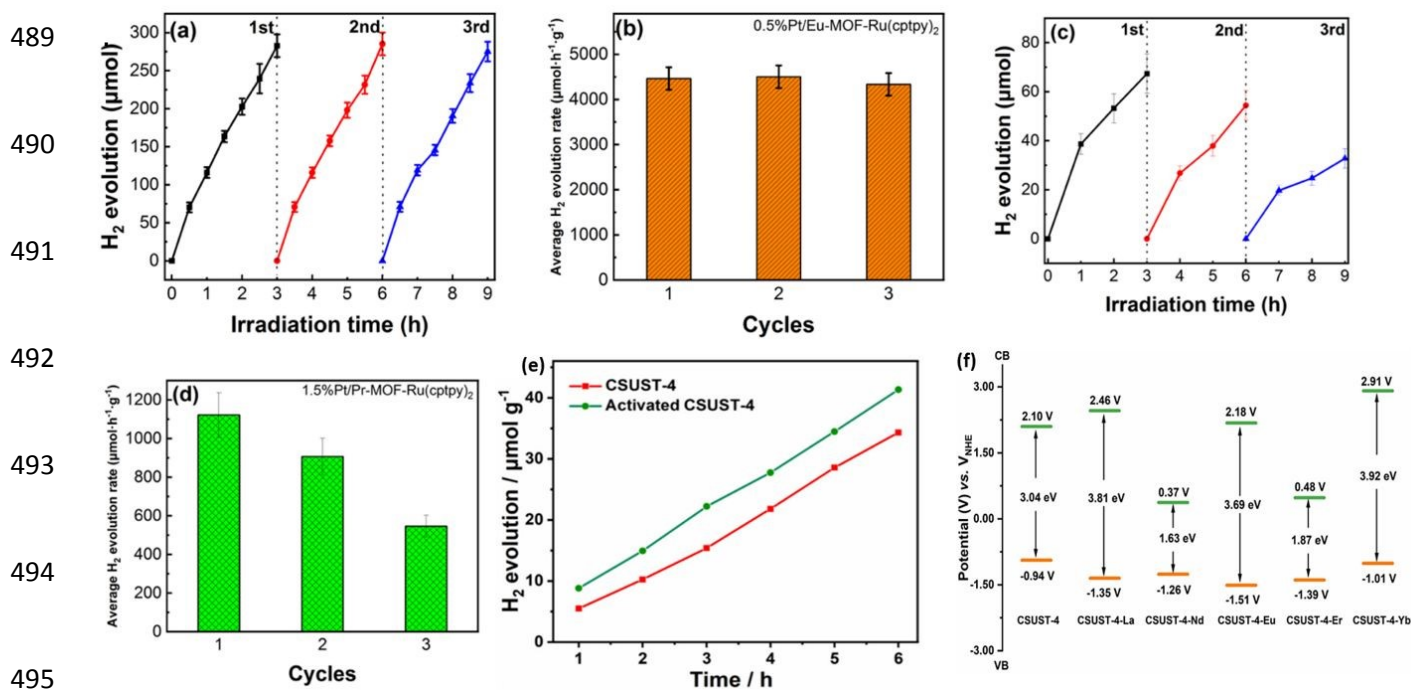
496 **Fig 7.** (a) Photocatalytic H$_2$ production amounts in the cycle test and (b) the average rate of

497 H$_2$ evolution during each cycle of 0.5% Pt/EuMOF-Ru(cptpy)$_2$. (c) Photocatalytic H$_2$

498 production amounts in the cycle test and (d) the average H$_2$ evolution rate during each

499 cycle of 1.5% Pt/ Pr-MOF-Ru(cptpy)$_2$. Reprinted with permission from ref.(164). Copyright

500 2023 ACS (e) Time course of photocatalytic H$_2$ evolution of CSUST-4 and activated CSUST-

501 4. (f) Energy diagrams of HOMO and LUMO levels of CSUST-4 and CSUST-Ln (Ln = La, Nd,

502 Eu, Er, Yb). Reprinted with permission from ref.(165). Copyright 2023 Wiley.

503   Another recent study by Gu et al., focuses on the photocatalytic hydrogen evolution (PHE)

504   activity and stability of a cerium-based MOF called CSUST-4, along with its lanthanide-

505   substituted variants (CSUST-4-Ln, where Ln = La, Nd, Eu, Er, Yb). CSUST-4 was synthesized

506   using a solvothermal method, yielding a 3D porous framework with significant potential for

507   photocatalysis due to its bandgap of 3.04 eV and n-type semiconductor properties. The

508   catalytic activity was assessed under simulated sunlight in the presence of triethylamine

509   (TEOA) as a sacrificial agent and Pt as a co-catalyst. Activated CSUST-4 showed an

510   improved hydrogen evolution of 41 μmol g^{-1} over 6 hours, compared to 34 μmol g^{-1} for the

511   as-synthesized version (Fig. 7e)(165)

512   This improvement is attributed to the exposure of open Ce (III) sites, which enhanced

513   interactions with water molecules, thereby boosting catalytic efficiency. When examining

514   the   stability   and   performance   of   lanthanide-substituted   variants,   CSUST-4-Nd

515   demonstrated the highest hydrogen evolution (71 μmol g^{-1} in 6 hours), followed by CSUST-

516   4-Er (61 μmol g^{-1}). These MOFs outperformed the base CSUST-4, while CSUST-4-Eu,

517   CSUST-4-La, and CSUST-4-Yb exhibited lower activities, likely due to their limited visible

518   light absorption and differing electronic properties. The band gap values of all the CSUST

519   MOFs studied is provided in Fig. 7f . The study highlights that the catalytic activity and

520   stability of these MOFs are closely tied to the specific lanthanide ion used, with Nd and Er

521   proving most effective for enhancing hydrogen production through water splitting (165).

522   **4.2. Doping metals.**

523   MOFs, characterized by their high surface area, tunable porosity, and structural diversity,

524   serve as an excellent platform for the incorporation of lanthanides. Recent studies have

525 shown that lanthanide doping modifies the band gap of the MOFs, enhances visible light

526 absorption, and facilitates the transfer of photogenerated carriers, thereby boosting the

527 overall photocatalytic activity(166,167). This subsection discusses the effects of doping

528 lanthanide metals in MOFs on their stability and efficiency in PHE through water splitting.

529 In 2019, Huang et al developed a new H_2BPDYC-Ce complex (UiO-67-Ce) by incorporating

530 Ce (IV) into UiO-67 at a 0.02 Ce/Zr ratio and replaced the H_2BPDC ligands with H_2BPYDC.

531 As a result, UiO-67-Ce exhibited a much higher PHE rate compared to UiO-67, with UiO-67-

532 Ce achieving 269.6 μmol g^{-1} h^{-1}, which is more than ten times higher than UiO-67's rate of

533 26.78 μmol g^{-1} h^{-1} under identical experimental conditions. This significant enhancement in

534 photocatalytic activity is attributed to the introduction of the Ce(IV) ion and the bpydc-Ce

535 ligand into the UiO-67 framework, which created new active sites and promoted efficient

536 energy transfer processes. Despite this remarkable increase in activity under UV/Vis

537 irradiation, neither UiO-67 nor UiO-67-Ce displayed any significant photocatalytic

538 hydrogen production activity under visible light alone (λ > 400 nm), indicating that their

539 performance is primarily driven by UV light (Fig. 8a). The ligand BPYDC-Ce displayed a

540 much stronger UV intensity than BPDC, indicating that Ce coordinates with the N atoms in

541 the ligand and not the carboxylate groups. An EPR signal with a g-value around 2.002,

542 indicating Zr^{3+} formation via the LMCT process, is observed in both UiO-67-Ce and UiO-67.

543 The signal is weaker in UiO-67-Ce, and no Zr^{3+} signal is detected in the dark for either

544 material (Fig. 8b). This suggests that the LMCT process under UV/Vis light is reduced in

545 UiO-67-Ce due to bpydc-Ce. The introduction of BPYDC-Ce is said to weaken LMCT and

546 promote energy transfer from BPDC to BPYDC-Ce, enhancing catalytic H_2 evolution (168).

547   The stability of UiO-67-Ce during photocatalytic reactions was confirmed by consistent

548   Ce/Zr ratios before and after testing, with no Ce ion leaching observed, indicating the

549   catalyst maintained its structural integrity. However, after 6 hours of continuous UV/Vis

550   irradiation, the H_2 evolution rate declined, suggesting reduced stability. XRD and SEM

551   analyses revealed this decline was due to decreased crystallinity and morphological

552   changes, with the cubic particles becoming irregular and larger. This structural degradation

553   was likely caused by hydroxyl nucleophile attack and mechanical stress during the

554   prolonged reaction(168).

555   In the year 2022, Yang et al., studied the photocatalytic performance of a novel Ce-based

556   MOF under visible light. The study presents the synthesis of a cerium-based metal-organic

557   framework (Ce-MOF) named Ce-TBAPy using a solvothermal method. XRD confirmed its

558   high crystallinity, showing Ce atoms coordinated with oxygen from the ligands. The

559   material displayed a cubic morphology with strong Ce-O interactions, contributing to

560   effective charge separation. Characterization techniques, including SEM, FT-IR, and NMR,

561   revealed uniform elemental distribution and high thermal stability. XPS analysis showed a

562   high concentration of Ce^{3+}, linked to oxygen vacancies that enhance photocatalytic

563   performance (Fig. 8c, 8d). UV-vis DRS indicated visible light absorption at 406 nm, with a

564   band gap of 2.75 eV. The material demonstrated efficient electron-hole pair separation and

565   improved photoreduction performance, particularly after loading a Pt co-catalyst. DFT

566   calculations confirmed that the –COO-Ce functional groups facilitate electron transfer and

567   inhibit recombination, boosting photocatalytic efficiency.

568
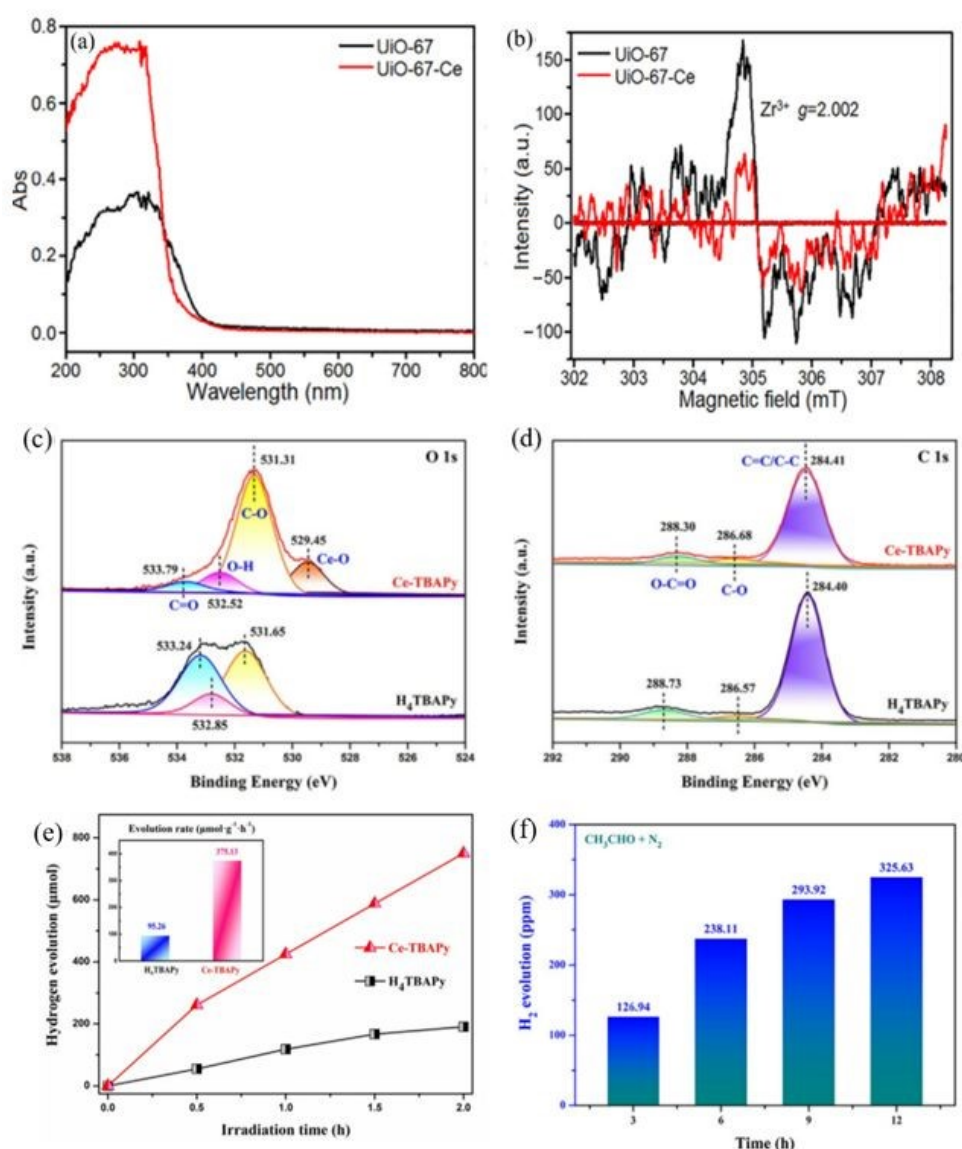
Fig 8. (a) UV/Vis DRS of UiO-67 and UiO-67-Ce, (b) EPR spectra of UiO-67 and UiO-67-Ce with the presence of UV/Vis illumination. Reprinted with permission from ref.(168) . Copyright 2019 Elsevier. High-resolution and separated peak curve XPS spectra of (c) O 1s and (d) C 1s. (e) Collaborative photocatalytic performance of H_2 liberation over Pt-loaded Ce-TBAPy in the CH_3CHO system under N_2 atmosphere. (f) Time course of H_2 liberation and evolution rate curve (inset) of samples. Reprinted with permission from ref. (169). Copyright 2022 Elsevier.

587 In terms of photocatalytic performance, Ce-TBAPy demonstrated exceptional hydrogen

588 production under visible light irradiation, achieving hydrogen evolution 3.94 times higher

589 than that of the untreated ligand (Fig. 8e). The material maintained its activity after three

590 rounds of testing, indicating excellent recyclability and stability (Fig. 8f). The bandgap

591 value of Ce-TBAPy (2.75 eV) and its conduction and VB positions made it well-suited for

592 water reduction, with efficient electron transfer facilitated by the Pt co-catalyst. The

593 overlapping structure of polycyclic aromatic conjugated polymers in the ligand further

594 promoted rapid migration of photo-induced electrons, contributing to the overall efficiency

595 of the photocatalytic process (169).

596 4.3. Dye-like MOFs

597 Given the advancements in light-harvesting MOFs, integrating organic dyes or dye-like

598 ligands as linkers in the construction of MOFs is a promising strategy. This leads to efficient

599 light sensitization and an increased number of photocatalytic sites within a single

600 structure, enhancing the MOF's photoactivity, stability, and insolubility. This approach

601 simplifies the system by eliminating the need for complex electron relay systems and co-

602 catalysts, making the MOF more effective at capturing and utilizing light (170–174). The

603 following section delves into the PHE performance of dye-like MOFs containing lanthanide

604 metals.

605 An organic dye-like MOF was reported by X. Sun et al. for the first time in 2015, where

606 3,3',5,5'-azobenzene tetracarboxylic acid was used as a linker in a Gd-MOF loaded with Ag

607 nanoparticles. The framework was found to be stable in the pH range of 3 to 14 for up to 48

608 h. UV-vis spectroscopy and electrochemical analysis reveal a broad absorption band and a

609 favorable energy gap (2.35 eV) for photocatalytic activity. The solid-state cyclic

610 voltammetry shows a suitable redox potential for proton reduction, confirming the MOF's

611 potential for hydrogen production (Fig. 9a).
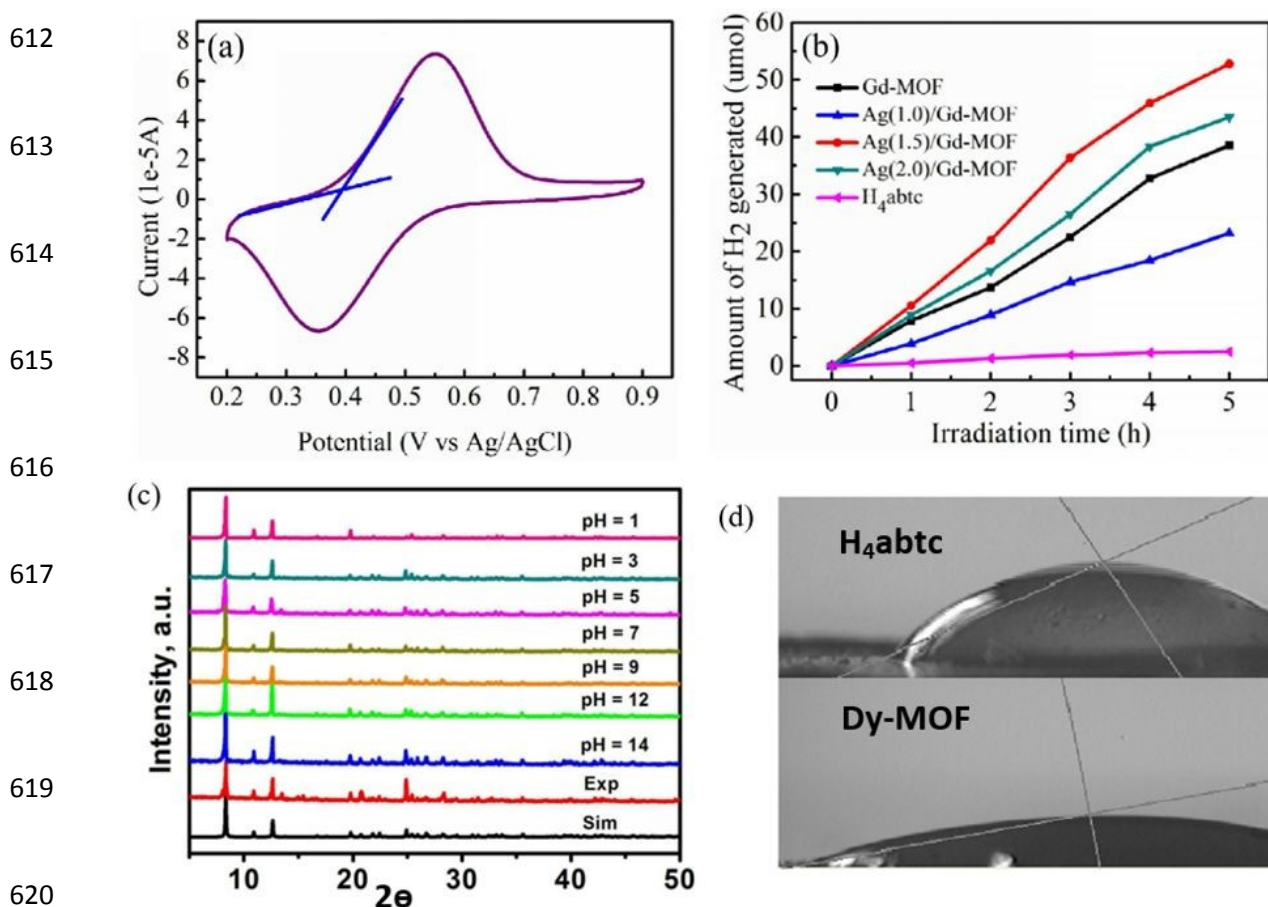
621 **Fig 9.** (a) CV curves of Gd-MOF. (b) Photocatalytic H_2 production under UV-vis light

622 irradiation over H_4abtc, Gd-MOF and Ag(X)/Gd-MOF. Reprinted with permission from ref.

623 (175). (c) The pH stability of dye-based Dy-MOF (d) The differences in hydrophilicity

624 between dye-based Dy-MOF and H_4abtc ligand using contact angle measurements.

625 Reprinted with permission from ref. (176). Copyright 2015 Royal Society of Chemistry.

626 In photocatalytic tests, Gd-MOF produced H_2 at a rate of 7.71 μmol h^{-1} g^{-1} under UV-vis

627 light without a co-catalyst, comparable to UiO-66. Adding Ag as a co-catalyst significantly

628 enhanced the performance. Ag-loaded Gd-MOF (1.5 wt%) achieved a hydrogen production

629 rate of 10.6 μmol h^{-1} g^{-1}, about 1.5 times higher than that of Gd-MOF alone (Fig. 9b). This

630 improvement is due to Ag's role in enhancing charge separation and light absorption

631 through surface plasmon resonance. The photocatalytic activity is maintained even after 5

632 hours of reaction, and the structure remains stable as confirmed by XRD. The

633 electrochemical impedance spectra and luminescence studies further support the

634 enhanced charge transfer and reduced recombination rates with Ag, leading to superior

635 photocatalytic performance (175).

636 In another similar work in 2018, Yu et al., synthesized a dye-based Dy-MOF through the

637 reaction of $DyCl_3 \cdot 6H_2O$ and Na_4abtc. The crystal structure, determined via X-ray analysis,

638 exhibits a novel 3D monoclinic framework with dimensions accommodating water

639 channels. The dye-based Dy-MOF demonstrates impressive photocatalytic performance

640 and stability. Under UV-vis light irradiation, it achieves a high hydrogen production amount

641 of 107.65 μmol g^{-1} over 5 hours, equivalent to 21.53 μmol g^{-1} h^{-1}. This rate surpasses that of

642 many MOF-based catalysts without dye-like ligands, such as UiO-66 and ZIF-8, though it is

643 somewhat lower compared to some porphyrin-based MOFs. The enhanced photocatalytic

644 efficiency of Dy-MOF is attributed to the inclusion of the dye-like ligand (H_4abtc), which

645 significantly improves light-harvesting capability. The UV-vis absorption spectrum of Dy-

646 MOF shows broad light absorption with an edge above 570 nm, corresponding to a π-π*

647 transition in organic ligands, indicating effective light capture. Additionally, the

648 incorporation of 0.8% Ag as a co-catalyst markedly boosts activity. The Ag acts as an

649 electron collector, enhancing charge separation and reducing electron-hole recombination,

650 which further increases the hydrogen production rate. In terms of stability, the dye-based

651 Dy-MOF exhibits robust thermal stability, maintaining its structural integrity up to 400°C

652 before collapsing, indicating its suitability for typical photocatalytic conditions (176).

653 Furthermore, the material demonstrates excellent water stability, retaining its structural

654 characteristics when soaked in solutions with pH values ranging from 3 to 14 for 48 h (Fig.

655 9c). This broad pH stability is essential for practical photocatalytic applications. Cycling

656 tests reveal that Dy-MOF maintains consistent hydrogen production performance up to the

657 third cycle, with no significant loss of activity. Post-reaction analysis by X-ray diffraction

658 (XRD) and FT-IR confirms that the material's structure remains largely unchanged,

659 underscoring its durability. Additionally, Dy-MOF's lower contact angle of 21.5°, compared

660 to 57.0° for the H_4abtc ligand, indicates higher hydrophilicity (Fig. 9d). This increased

661 hydrophilicity enhances water adsorption, which is beneficial for efficient proton reduction

662 during photocatalysis (176).

663 ### 4.4. Composites

664 Studies suggest that coupling MOFs with a catalytic semiconductor, results in an efficient

665 separation of charges and lead to an increase in the rate of H_2 evolution(177). $ZnIn_2S_4$ (ZIS)

666 based catalysts have an ability to absorb a broad spectrum of light (especially responsive to

667 visible light), maintain structural and functional integrity over a prolonged period and have

668 a tunable band gap energy that makes them suitable for application such as hydrogen

669 production through water splitting(178,179). However, electron hole recombination

670 occurs to a large extent in this material and in order to overcome this limitation various

671 modifications are done by forming composites with other metal oxides and sulfides(179–

672 182). In this context, ZIS decorated with Ln-MOF and Pt nanoparticles was reported in

673 2022 and its catalytic activity in water splitting was studied(183). The SBUs comprised of

674 Tm and Gd, were linked via 1,3,5-benzenetricarboxylic acid (BTC). The effect of Ln-MOF in

675 overall catalytic activity was studied by varying their % weight (1%,5% and 10%). The ZIS

676 spheres were clustered on the MOF microrods making the arrangement suitable for

677 electron transfer. The photo deposition of Pt nanoparticles along with the ZIS/(Tm,Gd)-

678 BTC caused a significant increase in the lower wavelengths of the visible region(183).

679 Increasing the % weight of the MOF in the ZIS composite showed a decrease in the intensity

680 of photoluminescence, while ZIS/1% (Tm, Gd)-BTC/Pt exhibited the highest intensity of

681 luminescence among the samples analyzed. Pt nanoparticles were shown to decrease the

682 rate of recombination and thus the photoluminescence; however, the addition of (Tm,Gd)-

683 BTC only had a minimal effect in decreasing the luminescence, suggesting a complex

684 interplay in the luminescence behaviour (Fig. 10a). Partial decomposition of ZIS and loss of

685 Pt was observed post-reaction through XRD and XPS studies. The efficiency of catalytic

686 hydrogen generation was analysed using various samples in the aqueous solution of

687 Na_2SO_3 and Na_2S (sacrificial electron donors). The samples used were pure ZIS, ZIS/Pt,

688 ZIS/x% (Tm, Gd)-BTC and ZIS/x% (Tm, Gd)-BTC/Pt. Pure ZIS and ZIS modified with (Tm,

689 Gd)-BTC at 1%, 5% and 10% by weight showed no activity in hydrogen generation while

690 the samples with Pt (ZIS/Pt and ZIS/x% (Tm, Gd)-BTC/Pt) were active in hydrogen

691 production. ZIS modified with 1% (Tm, Gd)-BTC/Pt produced hydrogen at a rate of 1945.5

692 $\mu mol\ g^{-1}\ h^{-1}$ when irradiated with UV-Vis light, which is much higher than that of pure ZIS,

693 which produced 49.07 $\mu mol\ g^{-1}\ h^{-1}$. Increasing the amount of the Ln-MOF, however,

694 decreased the photoactivity of the sample. The highest hydrogen production rate was

695 observed in the presence of both MOF and the Pt NPs, i.e., for 1g/L ZIS/1% (Tm, Gd)-

696 BTC/Pt where it produced a maximum of 2975 $\mu mol\ g^{-1}\ h^{-1}$ of hydrogen when irradiated

697 with UV-Vis. However, under visible light irradiation, its efficiency decreased as it produced

698 only 328.17 $\mu mol\ g^{-1}\ h^{-1}$ of hydrogen, which is lower than that of ZIS/Pt which produced

699 608.32 $\mu mol\ g^{-1}\ h^{-1}$. When tested for stability, ZIS/1%(Tm, Gd)-BTC/Pt displayed the

700 highest efficiency in the second cycle, producing 837 $\mu mol\ g^{-1}\ h^{-1}$ of hydrogen under visible

701 light (Fig. 10b). The efficiency is said to decrease in the subsequent cycles (183).

702 Since ZIS semiconductors face challenges such as low solar utilization, rapid recombination

703 of carrier charges, and low quantum yields, binary metal sulfides such as $Cd_xZn_{1-x}S$

704 especially $Cd_{0.2}Zn_{0.8}S$ have shown promising stability, excellent carrier transport capacity,

705 and adjustable band structure. $Cd_{0.2}Zn_{0.8}S$ has been identified to have the highest

706 photocatalytic activity among different compositions of $Cd_xZn_{1-x}S$ (184), however, its

707 application is limited because of the low separation and migration ability of

708 photogenerated electron hole pairs.

709 Recently, in 2024, a study by T.-T. Li et al., investigated the catalytic performance of

710 $Cd_{0.2}Zn_{0.8}S/Pr-NO_2$-TPTC. The lanthanide MOF is comprised of binuclear clusters

711 $[Pr_2(COO)_4]$ connected by multiple NO_2-TPTC^{4-} ligands, creating a three-dimensional

712 coordination framework. The NO_2-TPTC^{4-} ligands are said to form hydrogen bonds with the

713 lattice water in the solvent channels of the framework, thus enhancing absorption capacity

714 and promoting water splitting to improve catalytic hydrogen production. The UV-Vis DRS

715 shows absorption bands for Pr-NO_2-TPTC around 450 nm and for $Cd_{0.2}Zn_{0.8}S$ around 500

716   nm. When combining the Pr-NO$_2$-TPTC and the Cd$_{0.2}$Zn$_{0.8}$S in various ratios, especially with

717   a higher percentage of Pr-NO$_2$-TPTC, a red shift in the absorption peak is seen, indicating

718   improved light absorption and narrower band gap width (185).

719

720

721

722

723

724

725

726

727
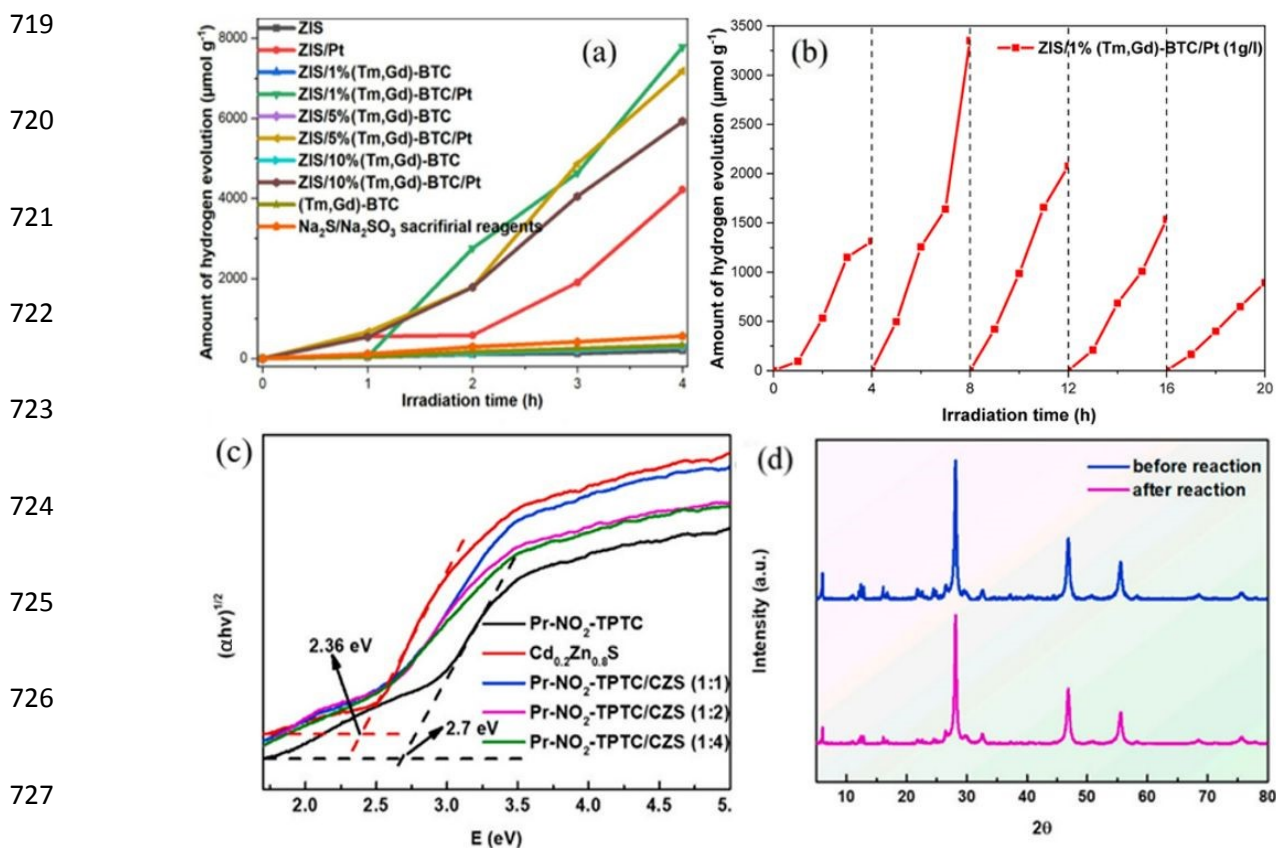
728   **Fig 10**. (a) Amount of produced hydrogen for all obtained samples under UV-Vis irradiation

729   (photocatalyst concentration 1.25 g/l) (b) Amount of produced hydrogen in five

730   photocatalytic cycles for ZIS/1% (Tm, Gd)-BTC/Pt (1 g/l) under visible irradiation (λ > 420

731   nm). Reprinted with permission from ref. (183). (c) Photonic energy map of the

732   photocatalysts, (d) PXRD patterns of Pr–NO$_2$–TPTC/CZS (1:1) before and after the

733   photocatalytic reaction. Reprinted with permission from ref. (185). Copyright 2024

734   Elsevier.

735 Pristine Pr-NO$_2$-TPTC shows no catalytic performance; however pure Cd$_{0.2}$Zn$_{0.8}$S produces

736 2712 µmol g^{-1} h^{-1} of hydrogen. The composite Pr-NO$_2$-TPTC/CZS in 1:1 ratio achieves the

737 highest hydrogen production rate of 6321 µmol g^{-1} h^{-1}, which is 2.33 times higher than that

738 of pure Cd$_{0.2}$Zn$_{0.8}$S. Other ratios, namely, 2:1 and 4:1, showed lower rates of hydrogen

739 generation. The photonic energy map of the compounds is given in Fig. 10c. The rate of

740 hydrogen produced by Cd$_{0.2}$Zn$_{0.8}$S was found to be 2092 µmol g^{-1} h^{-1} under visible light . Pr-

741 NO$_2$-TPTC/CZS in the 1:1 ratio, produced slightly lower but still significant amount of

742 hydrogen under visible light (5777 µmol g^{-1} h^{-1}). The catalytic performance of Pr-NO$_2$-

743 TPTC/CZS (1:1) was maintained for three consecutive uses, and there was no significant

744 deterioration of the materials seen (Fig. 10d). The Mott-Schottky analysis revealed a

745 positive slope indicating that the material is of n-type. In the photoluminescence studies,

746 the weakest emission at 560 nm which corresponded to Pr-NO$_2$-TPTC/CZS(1:1) showed a

747 low extent of electron-hole recombination. The transient photocurrent experiments

748 displayed a high response for the material, suggesting enhanced separation of

749 photogenerated carriers. The material also presented reduced charge transfer resistance

750 according to EIS. A heterojunction is said to form between Cd$_{0.2}$Zn$_{0.8}$S and Pr-NO$_2$-TPTC,

751 which promotes separation of the photogenerated charges and prolongs the carrier

752 lifetime. Under UV-Vis light irradiation of both Pr-NO$_2$-TPTC and Cd$_{0.2}$Zn$_{0.8}$S leads to the

753 generation of electron-hole pairs. The electrons from the LUMO of Pr-NO$_2$-TPTC migrates

754 to the CB of Cd$_{0.2}$Zn$_{0.8}$S thus reducing H$^+$ in the water to produce hydrogen. While the holes

755 move from the VB of Cd$_{0.2}$Zn$_{0.8}$S to the HOMO of Pr-NO$_2$-TPTC and are consumed by the

756 sacrificial agents (Na$_2$S and Na$_2$SO$_3$) present in the medium. The heterojunction that is

757 present in this composite inhibits electron-hole recombination, and hence there are a

758 greater number of electrons available for the reduction of protons (185).

759 4.5. Derivatives

760 It is an interesting fact that MOFs can also act as sacrificial templates, which can then be

761 converted into target multicomponent nanomaterials that serve as active photocatalysts.

762 This section throws light on how catalysts derived from Ln-MOFs perform in PHE

763 reactions, providing a clear insight on their efficiency and stability. For the first time, in

764 2019, Ce-doped g-C_3N_4 was reported, which was synthesized from MOFs made of Ti^{4+}, Zr^{4+},

765 Ce^{3+}, and Er^{3+} and then doped with four different amounts of Ce^{3+}, denoted as xCe-C_3N_4 (x =

766 0.010, 0.015, 0.030, or 0.090 mol). Ce-C_3N_4 was modified using NH_4F, $NaHCO_3$, or cellulose

767 acetate, producing NF-CN (NH_4F-modified), NHC-CN ($NaHCO_3$-modified), and CA-CN

768 (cellulose acetate-modified) Ce-C_3N_4. Among the various Ce^{3+} concentrations tested, Ce-

769 C_3N_4 with 0.015 mol Ce^{3+} exhibited the highest photocatalytic activity. This can be

770 attributed to the optimal doping level of Ce^{3+}, which enhances the photocatalytic

771 performance without causing excessive amorphization or disrupting the C_3N_4 lattice. At

772 this concentration, Ce^{3+} effectively reduces the bandgap energy and enhances the

773 separation efficiency of photoexcited electron-hole pairs. This leads to a more efficient

774 photocatalytic process, as evidenced by the highest hydrogen production rates observed. In

775 contrast, higher concentrations of Ce^{3+} (0.030 and 0.090 mol) result in decreased

776 photocatalytic activity. This decline is due to the interference with the formation of the

777 C_3N_4 structure and the introduction of excessive amorphous phases, which negatively

778 impacts the material's ability to absorb light and facilitate charge separation (186).

Energy Advances Accepted Manuscript

Energy Advances Accepted Manuscript
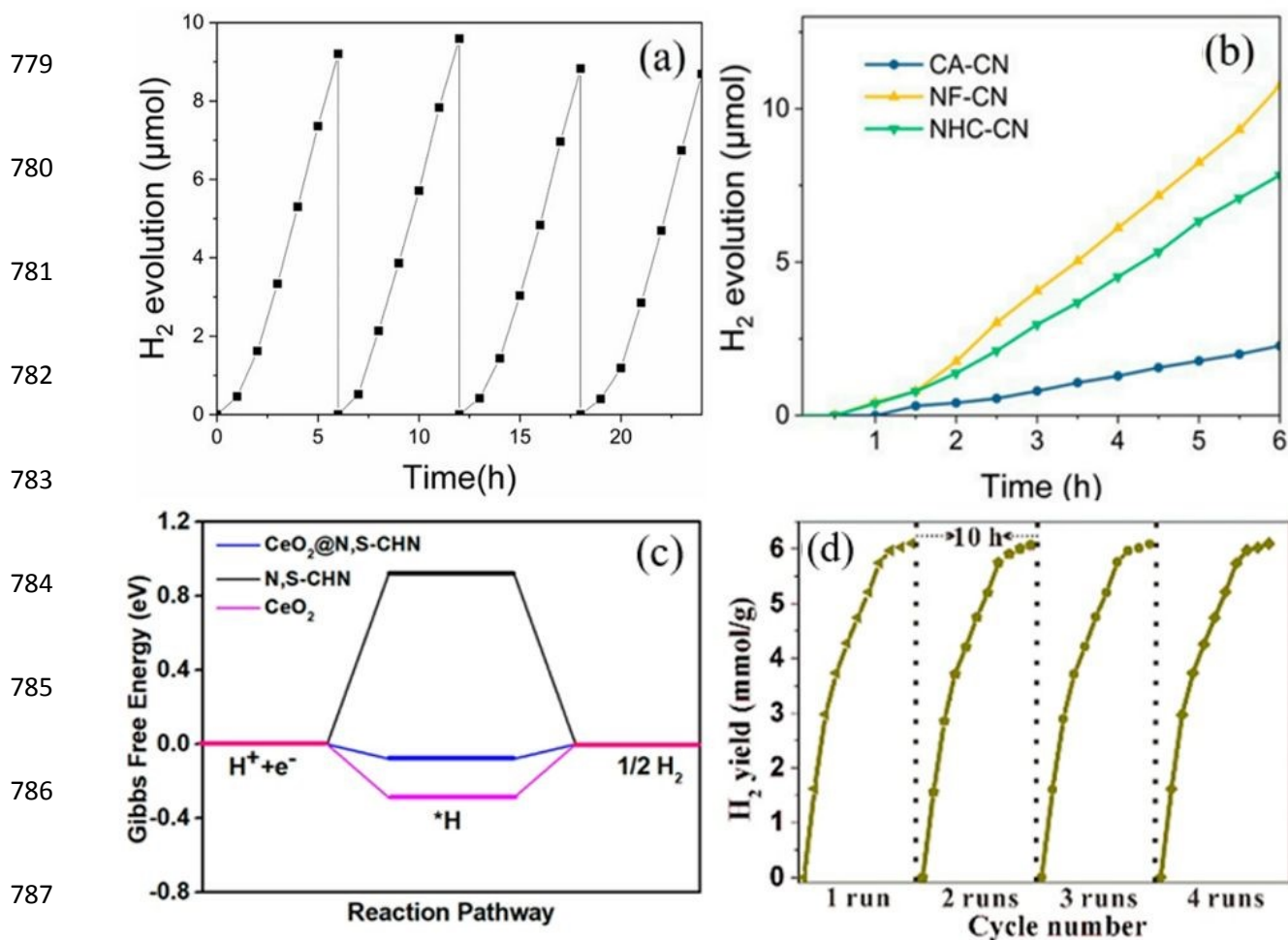
Fig. 11. (a) The 24 h cyclic measurement of H_2 evolution from $0.015Ce-C_3N_4$. (b) Photocatalytic H_2 evolution of CA-CN, NF-CN, and NHC-CN. Reprinted with permission from ref. (185). Copyright 2019 MDPI (c) Gibbs free energy profile of the hydrogen evolution reaction for $CeO_2@N,S–C$ HN (blue), $N,S–C$ (black), and CeO_2 with the (111) crystal plane (pink). (b) The 40h cyclic measurement of H_2 evolution from $CeO_2@N,S–C$ HN. Reprinted with permission from ref. (185). Copyright 2019 ACS.

The sample demonstrates excellent stability under visible light irradiation for over 24 h across four cycles (Fig. 11a). The slight decrease in activity is due to TEOA consumption. Overall, $0.015Ce-C_3N_4$ shows robust and consistent performance, making it suitable for practical applications. The modifications using $NaHCO_3$ and cellulose acetate also lead to

798 significant improvements in photocatalytic activity. Cellulose acetate-modified samples, in

799 particular, exhibit increased visible light absorption and better light-harvesting efficiency,

800 contributing to improved photocatalytic performance. On the other hand, the incorporation

801 of fluorine shifts both the VB and CB to higher energy levels, which enhances the

802 photocatalytic activity by improving charge carrier dynamics (Fig. 11b). The stability of

803 modified samples, including those doped with NH_4F, $NaHCO_3$, and cellulose acetate, aligns

804 with the trends seen in base $Ce-C_3N_4$. These modifications generally enhance morphological

805 stability, with NH_4F creating finer fibres and cellulose acetate and $NaHCO_3$ improving

806 structural robustness. Consequently, these modifications contribute to more consistent and

807 reliable photocatalytic activity(186).

808 In the following year, Hao et al., successfully synthesized N,S-codoped C-encapsulated CeO_2

809 with a hinge-like structure through the thermal decomposition of sulfanilic acid-modified

810 Ce-based MOFs. The CeO_2@N,S−C HN catalyst demonstrated outstanding photocatalytic

811 performance in PHE reactions. Its mass-normalized hydrogen production rate reached 555

812 μmol h^{-1} g^{-1}, surpassing that of CeO_2@C HN (405 μmol h^{-1} g^{-1}), CeO_2 HN (325 μmol h^{-1} g^{-1}),

813 and commercial CeO_2 (195 μmol h^{-1} g^{-1}) The Gibbs free energy profile of the PHE reaction

814 for all three compounds is given in Fig. 11c. This exceptional activity is largely due to the

815 combination of the N,S-codoped carbon layer and the hinge-like porous structure of the

816 catalyst. The N,S-codoped carbon enhances visible light absorption and facilitates efficient

817 separation and transport of photogenerated charge carriers. The hinge-like structure

818 further improves light trapping and enhances the photocatalytic process by allowing

819 multiple reflections and increasing the interaction surface. Regarding stability,

820 CeO_2@N,S−C HN exhibited impressive performance consistency over multiple cycles (Fig.

Energy Advances Accepted Manuscript

821   11d). In PHE tests under simulated sunlight irradiation, the catalyst maintained high

822   activity over four cycles, with no significant loss in performance.

823   The stability was assessed through repeated cycling, and the catalyst showed negligible

824   deactivation, maintaining its structural and compositional integrity throughout.

825   Characterization techniques, XRD, SEM, and EDX, confirmed that the catalyst retained its

826   morphology and elemental distribution after several cycles. This robust stability is

827   attributed to the effective encapsulation of CeO_2 nanoparticles by the N,S-doped carbon

828   layer, which protects the core material from degradation and preserves its catalytic

829   properties over extended use. Overall, the $CeO_2@N,S-C$ HN catalyst combines high

830   photocatalytic efficiency with long-term stability, making it a promising candidate for

831   sustainable photocatalytic applications (187).

832   4.6. Photosensitizers

833   It is interesting that Ln-MOFs find application as photosensitizers in addition to all the

834   aforementioned applications in PHE. This section summarizes the use of Ln-MOFs as

835   photosensitizers in aiding the production of hydrogen through water splitting. In a 2016

836   study by P. Wu et al., the photosensitizing properties of a Gd-MOF featuring the TCA^{3-}

837   ligand were extensively explored. The Gd-TCA framework benefits from the unique

838   characteristics of Gd(III), which avoids unwanted energy transfer due to its lack of low-

839   energy levels below 32,000 cm^{-1}. This makes it particularly suited for photosensitizing

840   applications. The framework's large surface area and porous structure enhance its stability

841   and longevity in aqueous environments, facilitating processes such as hydrogen evolution.

842   The UV-Vis spectrum of Gd-TCA shows a significant π-π* transition at 350 nm, while its

843 redox potentials are 0.82 V in the ground state and -2.30 V in the excited state. This

844 indicates a strong capacity for electron transfer, crucial for effective hydrogen production.

845 The study assessed the framework's performance with two different catalytic systems: a

846 [Fe-Fe]-based hydrogenase mimic (C1) and a cobalt complex, $[Co(bpy)_3]Cl_2$ (C2).

847 For the [Fe-Fe]-based catalyst (C1), the addition of $NiPr_2EtH.OAc$ as a sacrificial electron

848 donor led to increased hydrogen production rates with higher catalyst concentrations.

849 Initially, hydrogen production rates showed first-order dependence on C1 concentration

850 (Fig. 12a), but this linear increase stalled at concentrations above 10 mM due to C1's poor

851 solubility. After 6 hours of irradiation, a notable drop in hydrogen production indicated

852 potential decomposition of a system component. However, reintroducing C1 and

853 $NiPr_2EtH.OAc$ to the filtered MOF successfully resumed hydrogen production. Over a 40-

854 hour period with four rounds of continuous irradiation, a total of 15 mL of hydrogen was

855 produced. In contrast, the cobalt-based catalyst, $[Co(bpy)_3]Cl_2$ (C2) demonstrated

856 significant quenching of Gd-TCA's emission but showed notable catalytic activity. Under

857 alkaline conditions, Gd-TCA with C2 achieved a turnover frequency of 320 h^{-1} per molecule

858 of C2 within the first hour and a quantum yield of 0.21%. While the hydrogen evolution

859 rate increased with C2 concentration up to 50 μM, further increases did not enhance the

860 rate linearly, likely due to catalyst decomposition (Fig. 12b). As with C1, the system's

861 activity was restored with the addition of fresh C2 and base. This system also

862 demonstrated impressive longevity, producing 22 mL of hydrogen over 20 hours and five

863 rounds.

864
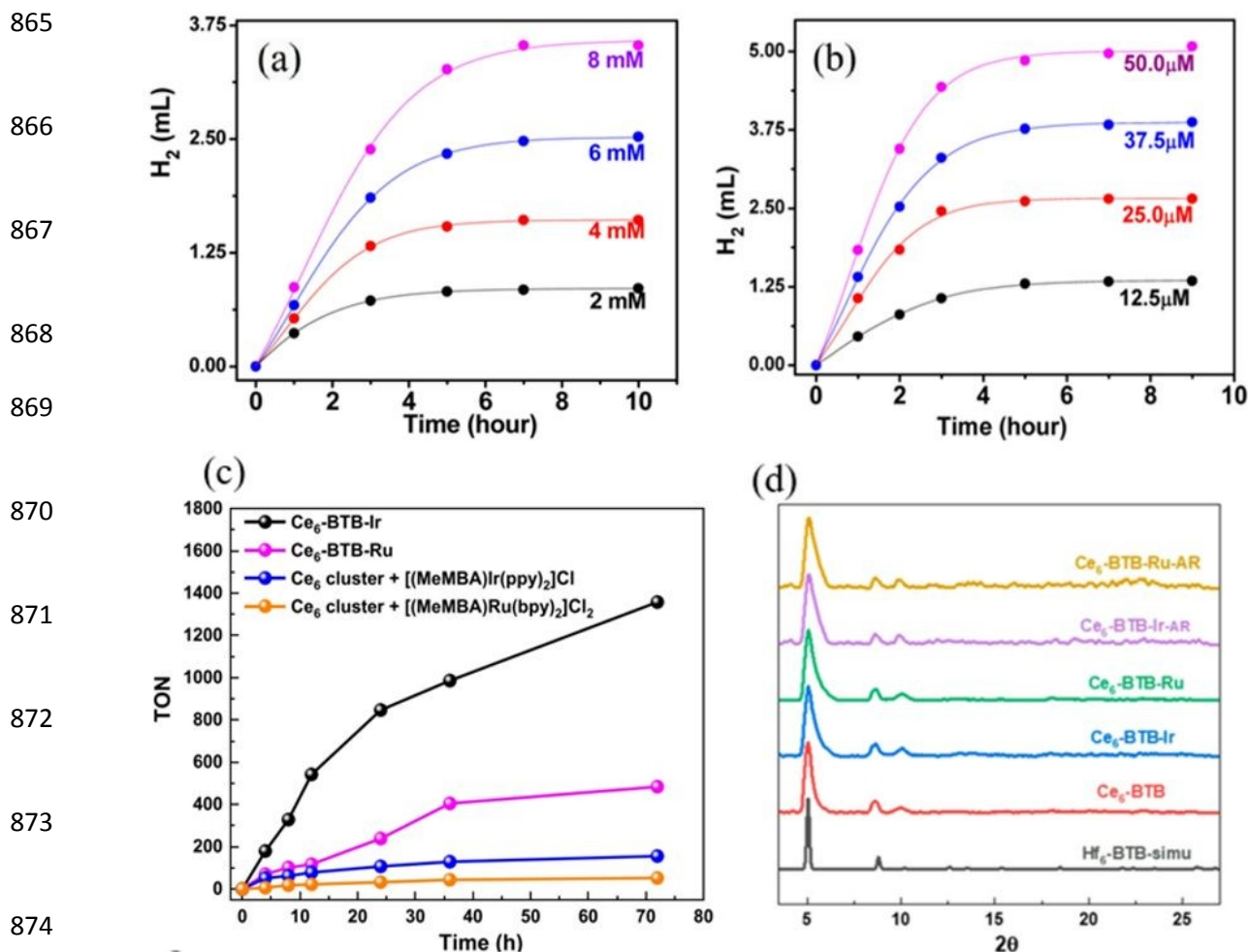
Fig 12. (a) H_2 evolution of Gd-TCA (1 mg), in 5 mL of solution containing $NiPr_2EtH \cdot OAc$ (0.8 M) and C1 with various concentrations. (b) H_2 evolution of Gd-TCA (1 mg), in 5 mL of a solution containing Et_3N (2.5%) and C2 ($[Co(bpy)_3]Cl_2$) with various concentrations. Reprinted with permission from ref. (188). Copyright 2016 ACS. (c) Time-dependent PHE TONs of Ce_6-BTB-Ir and Ce_6-BTB-Ru along with homogeneous controls (d) PXRD patterns of Ce_6- BTB (red), Ce_6-BTB-Ir (blue), and Ce_6-BTB-Ru (green), Ce_6-BTB-Ir after reaction (purple), and Ce_6-BTB-Ir after reaction (khaki) in comparison to that simulated for Hf6-BTB MOL (black). Reprinted with permission from ref. (134). Copyright 2020 ACS.

883   Additionally, Gd-TCA was utilized in the form of films supported by α-Al$_2$O$_3$, known for its

884   high affinity towards carboxylic groups. The initial hydrogen production rate from a 1.5 ×

885   0.5 cm^2 film was 1.71 mL h^{-1}, yielding 3.8 mL of hydrogen in the first 5 hours under alkaline

886   conditions with 50 µM C2. The film-based system maintained hydrogen production for over

887   40 hours, generating a total of 33.5 mL of hydrogen. This study marks the first reported use

888   of MOF films for the photochemical reduction of water, highlighting the Gd-TCA

889   framework's exceptional performance and stability in both powder and film forms (188).

890   In addressing limitations of traditional MOFs in photocatalysis, such as light scattering at

891   the nanoscale and inefficient light penetration in bulk forms, researchers have developed

892   metal-organic layers (MOLs). MOLs, as monolayer versions of MOFs, offer improved

893   photocatalytic performance by reducing light scattering and enhancing diffusion of

894   reaction components. This innovation aims to overcome the constraints imposed by MOF

895   symmetry and channel diffusion issues. The first Ce-based MOL was successfully

896   synthesized and studied by Song et al., in 2020. The SBUs are made of Ce$_6$ clusters, and they

897   are linked using BTB molecules (134). The MOLs are capped with photosensitizing

898   molecules such as [(HMBA)Ir(ppy)$_2$]Cl and [(HMBA)Ru(bpy)$_2$]Cl$_2$. The study evaluates the

899   PHE activities of two metal-organic layers (MOLs): Ce$_6$-BTB-Ir and Ce$_6$-BTB-Ru. These

900   MOLs were tested in an oxygen-free acetonitrile solution with acetic acid as the proton

901   source and 1,3-dimethyl-2-phenyl-2,3-dihydro-1H-benzo[d]imidazole (BIH) as the

902   sacrificial agent. The performance was assessed by quantifying hydrogen production

903   through gas chromatography. Both Ce$_6$-BTB-Ir and Ce$_6$-BTB-Ru exhibited impressive PHE

904   activities, with turnover numbers (TONs) of 1357 and 484, respectively (Fig. 12c),

905   following 72 hours of photoirradiation using a solid-state plasma light source. The

906 apparent quantum yields were 4.8% for Ce$_6$-BTB-Ir and 3.8% for Ce$_6$-BTB-Ru. These results

907 highlight the superior photocatalytic performance of these MOLs compared to their

908 homogeneous counterparts, which demonstrated significantly lower TONs. (134).

909 Stability was a crucial aspect of the study. Both Ce$_6$-BTB-Ir and Ce$_6$-BTB-Ru maintained

910 their structural integrity after PHE, as evidenced by consistent PXRD patterns (Fig. 12d)

911 and HRTEM images, with less than 3% leaching of Ce into the solution. The MOLs also

912 retained their photocatalytic activity over at least three consecutive runs, demonstrating

913 their durability under reaction conditions. This structural stability and enduring activity

914 underscore the effectiveness of MOLs in photocatalytic applications (134).

915 The summary of all Ln-MOFs discussed above has been given in Table 3. Apart from all

916 these studies reported regarding the efficiency of Ln-MOFs in the photocatalytic water-

917 splitting processes, various computational studies suggest that Ln-MOFs are promising

918 candidates to be employed in photocatalytic water-splitting. For instance, in 2020

919 Anderson et al., presented two series of lanthanide-based MOFs (Ln-SION1 and Ln SION-2),

920 and found that Ln-SION1 series shows photoconductivity due to its desirable orbital

921 structure. They conclude that the later members of the series have the potential to act as

922 photocatalysts for water-splitting, with the help of a photocatalyst (189). Additionally,

923 Hidalgo-Rosa et al., in 2023, discuss the significance of functional groups on enhancing the

924 light-harvesting nature of rare earth MOFs and suggest that these materials could show

925 photocatalytic properties upon solar light irradiation (190). All these studies emphasize

926 that numerous opportunities lie ahead of researchers in the field of photocatalytic water-

927 splitting when it comes to lanthanide-based MOFs. Furthermore, their structural tunability

928 and reusability align with the goals of sustainable hydrogen production. However,

929 economic feasibility remains a significant challenge. The high cost of lanthanides, due to

930 their scarcity and complex extraction processes, and the intricate synthesis methods

931 required for Ln-MOFs, make them expensive to produce. Scaling up production while

932 maintaining performance is also challenging, further hindering their large-scale adoption.

933 Additionally, these materials face competition from more cost-effective alternatives such as

934 transition metal-based catalysts like TiO_2 or ZnO which are widely available and easy to

935 produce. Real-world deployment of Ln-MOFs requires further validation of their efficiency

936 and stability under practical conditions, as laboratory performance may not directly

937 translate to operational environments. Despite these challenges, strategies such as material

938 optimization—using mixed-metal MOFs or doping to reduce lanthanide content—can

939 lower costs while maintaining functionality. Advances in synthesis techniques, including

940 greener and scalable methods, along with recycling and recovery of lanthanides from spent

941 MOFs, could further enhance economic viability. As global demand for sustainable energy

942 solutions grows, increased research and industrial collaboration may drive cost reductions

943 and facilitate commercialization. Although currently less economically competitive, Ln-

944 MOFs remain a promising avenue for green hydrogen production with further

945 technological and economic advancements.

S.No.	Ln-MOF Photocatalyst	Surface area of catalyst (m^2g^{-1})	SDs and their concentration	Light Sources	PHE rate $(\mu molg^{-1}h^{-1})$	TON	AQE	Stability	References
1	UiO-66(Ce/Zr/Ti)	1019	Methanol	150 mW cm^{-2} Xe lamp (λ>450 nm)	17.7 μmol g^{-1}	-	5.5%	Stable upto 2 cycles	(157)
2	0.5%Pt/Eu-MOF-Ru(cptpy)$_2$	4.0	AA (0.1 M)	300 W Xe lamp ($\lambda \geq$ 420 nm)	4373 μmol g^{-1}	-	0.79%	Stable upto 3 cycles (9h)	(164)
3	1.5%Pt/Pr-MOF-Ru(cptpy)$_2$	9.9	AA (0.1 M)	300 W Xe lamp ($\lambda \geq$ 420 nm)	1047 μmol g^{-1}	-	-	Not very stable (3h)	(164)
4	CSUST-4-Nd	-	TEOA (0.65 M)	300 W Xe lamp	71 μmol g^{-1}	-	-	Moderate thermal stability	(165)
5	CSUST-4-Er	-	TEOA (0.65 M)	300 W Xe lamp	61 μmol g^{-1}	-	-		(165)

6	Activated CSUST-4	-	TEOA (0.65 M)	300 W Xe lamp	41 µmol g^{-1}	-	-	(upto 350 $^\circ$C)	(165)
7	UiO-67-Ce	1,545	Methanol	300 W Xe lamp	269.6 µmol g^{-1}	-	-	Stable upto 6h	(168)
8	Ce-TBAPy	-	TEOA (0.65 M)	300 W Xe lamp ($\lambda \geq 420$ nm)	375.1 µmol g^{-1}	-	-	Good stability and recyclability upto 12 h	(169)
7	Ag(1.5)/Gd-ABTC	-	TEOA (~3 M)	300 W Xe lamp	10.6 µmol g^{-1}	-	-	Stable for 48h at pH 3-14	(175)
8	0.8Pt/Dy-ABTC	-	TEOA (2.26 M)	300 W Xe lamp ($\lambda > 320$ nm)	21.5 µmol g^{-1}	-	-		(176)
9	ZIS/1% (Tm, Gd)-BTC/Pt	-	Na_2SO_3/Na_2S (0.25 M)	300 W Xe lamp ($\lambda \geq 420$ nm)	1945.5 µmol g^{-1}	-	-	Poor stability	(183)
10	Pr–NO_2–	3.4480	Na_2SO_3/Na_2S	Full light	6321 µmol	-	-	Stable upto 12 h	(185)

51

	TPTC/CZS (1:1)				g^{-1}				
11	CeO$_2$@N,S-CHN	26.9	-	Full light	555 µmol g^{-1}	-	-	Good stability upto 40h	(186)
12	Gd-TCA/C1	-	Nipr$_2$EtH.OAc (0.8 M)	500 W Xe lamp	16.7 µmol g^{-1}	-	-	Poor stability	(188)
13	Gd-TCA/C2	-	Et$_3$N (0.179 M)	500 W Xe lamp	49.1 µmol g^{-1}	-	0.21%	Poor stability	(188)
14	Gd-TCA Film	-	Et$_3$N (0.179 M)	500 W Xe lamp	76.3 µmol g^{-1}	-		Stable upto 40 h	(188)
15	Ce$_6$-BTB-Ir	-	BIH	13.9 W 350–700 nm solid-state plasma light source	-	1357	4.8%	Good stability	(134)

16	Ce$_6$-BTB-Ru	-	BIH	13.9 W 350–700 nm solid-state plasma light source	-	484	3.8%	Good stability	(134)

946   **Table 3.** Summary of Ln-MOFs and their derivatives discussed in this review.

947 **5. CONCLUSIONS AND FUTURE OUTLOOK**

948 Lanthanide-MOFs have emerged as promising materials for photocatalysis in recent years,

949 particularly in hydrogen production via PHE. The unique properties of lanthanides, such as

950 their distinctive luminescence and the ability to finely tune their electronic and optical

951 characteristics, have driven significant advancements in this field. Early research on the

952 luminescence of Ln-MOFs provided insights into energy transfer mechanisms, revealing

953 how these frameworks harness light and convert it into usable energy, which is crucial for

954 enhancing photocatalytic efficiency.

955 Ln-MOFs have gained significant attention in photocatalysis, particularly for hydrogen

956 production via water splitting, due to their unique ability to form mixed-metal frameworks

957 without altering the MOF structure. This flexibility is made possible by the similar crystal

958 structures of adjacent rare earth ions, which allows for the introduction of active sites and

959 the enhancement of catalytic performance through electron relay between different metal

960 nodes. The result is a material that can be finely tuned for optimal photocatalytic efficiency.

961 Recent advancements in the field have demonstrated that trimetallic Ln-MOFs, which

962 integrate three different metals into a single framework, can achieve a significant boost in

963 catalytic activity compared to their single-metal counterparts. This improvement is

964 primarily due to the broader absorption spectrum and reduced band gap that these mixed-

965 metal systems offer, enabling more efficient light harvesting and energy transfer.

966 Additionally, lanthanide doping, particularly in combination with Pt co-catalysts, has

967 proven to be an effective strategy for further enhancing the photocatalytic efficiency and

968 stability of these materials. The introduction of Pt helps to improve charge separation and

969 transfer, leading to more efficient hydrogen production. To overcome traditional

970 limitations of MOFs, such as light scattering and inefficient light penetration, researchers

971 have developed MOLs. These thinner materials, combined with photosensitizing molecules,

972 exhibit high PHE activities while maintaining their structural integrity over multiple cycles.

973 Gd-based Ln-MOFs have also shown promise in this area, demonstrating effective electron

974 transfer and strong photocatalytic activity, resulting in sustained hydrogen production

975 over extended periods. Ln-MOFs have also been used as sacrificial templates to create more

976 efficient photocatalysts. These materials exhibit enhanced visible light absorption and

977 charge separation, leading to superior photocatalytic activity and stability. Furthermore,

978 the combination of Ln-MOFs with catalytic semiconductors has shown significant potential

979 in further enhancing hydrogen production. Ln-MOF-semiconductor composites take

980 advantage of the synergistic effects of both materials, resulting in improved light

981 absorption, charge separation, and overall photocatalytic efficiency. In addition, numerous

982 studies support the fact that lanthanide-based MOFs show efficient LMCT and up

983 conversion properties. Nd based complexes and MOFs have shown photon up conversion

984 properties through which they emit blue light (191–193). Up-conversion displayed by

985 lanthanides represents a powerful approach to enhance photocatalytic water-splitting.

986 Overall, incorporation of lanthanides into frameworks increase their photocatalytic

987 activity, somewhere from 2.3 in Ui0-67-Ce to 10 times in Pr–NO2–TPTC/CZS (1:1), by

988 altering their band gap values and hence improving light absorption. Among all the

989 lanthanides discussed in this review, Ce, Eu, Pr, Tm and Gd outperform other lanthanides

990 by improving charge separation and light absorption, owing to their unique electronic

991 structure. Though almost all of the studies involve the use of SDs, Ce-doped g-CN seems to

992   have performed the best in our opinion, exhibiting excellent hydrogen production rate in

993   the absence of an SD and appreciable stability up to 40 h. in addition to the Ce-doped g-CN ,

994   Pr–NO2–TPTC/CZS (1:1) and Eu-MOF-Ru(cptpy)$_2$, offer notable efficiency and hence can be

995   used for practical application. The incorporation of dye-like ligands, multiple lanthanides,

996   and semiconductors are indeed innovative approaches to enhance the PHE performance of

997   Ln-MOFs.

998   With all this being said, future research on Ln-MOFs should focus on several key areas to

999   fully unlock their potential in photocatalysis, particularly for hydrogen production. One

1000   critical area is enhancing the quantum efficiency of Ln-MOFs through optimizing photon

1001   absorption, energy transfer processes, and minimizing non-radiative losses, which will be

1002   crucial for boosting the overall photocatalytic performance of these materials. Exploring

1003   new lanthanide elements and their combinations within MOFs is another promising

1004   avenue. Less commonly studied lanthanides could offer unique optical and electronic

1005   properties, potentially leading to improved band gaps and more efficient energy transfer

1006   mechanisms. The creation of mixed-metal MOFs, leveraging the identical crystal structures

1007   of adjacent lanthanide ions, allows for the introduction of active sites and enhances

1008   catalytic performance through electron relay between different metal nodes. The

1009   integration of Ln-MOFs with emerging technologies, such as artificial photosynthesis and

1010   solar fuel production, could open new avenues for clean energy applications. However,

1011   most of the Ln-MOFs still face challenges in effectively utilizing sunlight. Most of the Ln-

1012   MOFs reported derive their photocatalytic activity to a major extent from UV light that

1013   constitutes only about 5%. Hence the visible-light response of these catalysts has to be

1014   improved. Furthermore, improving the stability and durability of Ln-MOFs under

1015   prolonged irradiation and harsh reaction conditions remains a challenge. Future research

1016   should focus on developing more robust materials that maintain their performance over

1017   extended periods, addressing issues like structural degradation and the stability of doped

1018   and composite MOFs. Furthermore, with the advancements in artificial intelligence (AI)

1019   technologies, machine learning (ML) has become a great tool with vast applications. ML has

1020   the potential to revolutionize the design of Ln-MOFs for PHE. By rapidly predicting key

1021   properties such as band gaps, charge carrier mobility, and photocatalytic activity, ML

1022   models can accelerate the screening and optimization of Ln-MOFs. These models can be

1023   trained on existing data from quantum chemical calculations like density functional theory

1024   or experimental results, allowing researchers to explore vast compositional spaces and

1025   identify the most promising materials. By integrating ML with high-throughput

1026   experiments, material synthesis, and computational chemistry, researchers can

1027   significantly reduce the time and cost involved in discovering and optimizing new Ln-MOFs

1028   for hydrogen production. This interdisciplinary approach fosters the development of high-

1029   performance photocatalysts, making ML an essential tool in advancing sustainable energy

1030   solutions. Finally, assessing the environmental and economic impacts of Ln-MOFs in large-

1031   scale applications will be crucial for ensuring their sustainability and informing their

1032   adoption in practical systems for energy and environmental applications. Developing

1033   frameworks resistant to hydrolytic and photochemical degradation will enhance stability.

1034   Replacing expensive co-catalysts like Pt with earth-abundant alternatives (e.g., Ni, Co) is

1035   crucial for cost reduction. Research into dye-based MOFs and composites can improve

1036   visible-light activity, while scalable and cost-effective synthesis methods will facilitate the

1037   transition from lab-scale research to industrial applications. Continued research and

1038   development in this field, focusing on new materials, synthesis methods, and real-world

1039   applications, will be crucial for unlocking the full potential of Ln-MOFs and addressing

1040   global energy and environmental challenge.

1041   **ACKNOWLEDGEMENTS**

1046   **CREediT STATEMENT**

1047   **P Danita Patricia:** Conceptualization, Writing-Original draft.

1048   **Rajadurai Vijay Solomon:** Conceptualization, Supervision, Draft editing.

1049   **COMPETING INTERESTS**

1050   The authors declare that they have no competing interests.

1051   **REFERENCES**

1052   1.   Francis JA, Vavrus SJ. Evidence linking Arctic amplification to extreme weather in mid-latitudes.
1053   Geophys Res Lett. 2012 Mar 28;39(6).

1054   2.   Acar C, Dincer I. Review and evaluation of hydrogen production options for better environment. J
1055   Clean Prod. 2019 May;218:835–49.

1056   3.   Abdalla AM, Hossain S, Nisfindy OB, Azad AT, Dawood M, Azad AK. Hydrogen production,
1057   storage, transportation and key challenges with applications: A review. Energy Convers Manag.
1058   2018 Jun;165:602–27.

1059   4.   Tarhan C, Çil MA. A study on hydrogen, the clean energy of the future: Hydrogen storage
1060   methods. J Energy Storage. 2021 Aug 1;40:102676.

Energy Advances Accepted Manuscript

1061 5. Reddy SN, Nanda S, Vo DVN, Nguyen TD, Nguyen VH, Abdullah B, et al. Hydrogen: fuel of the near
1062   future. In: New Dimensions in Production and Utilization of Hydrogen. Elsevier; 2020. p. 1–20.

1063 6. Bicer Y, Dincer I. Life cycle evaluation of hydrogen and other potential fuels for aircrafts. Int J
1064   Hydrogen Energy. 2017 Apr 20;42(16):10722–38.

1065 7. Chiesa P, Lozza G, Mazzocchi L. Using Hydrogen as Gas Turbine Fuel. J Eng Gas Turbine Power.
1066   2005 Jan 1;127(1):73–80.

1067 8. Szwaja S, Grab-Rogalinski K. Hydrogen combustion in a compression ignition diesel engine. Int J
1068   Hydrogen Energy. 2009 May;34(10):4413–21.

1069 9. Arat HT, Baltacioglu MK, Aydin K, Özcanli M. Experimental investigation of using 30HCNG fuel
1070   mixture on a non-modified diesel engine operated with various diesel replacement rates. Int J
1071   Hydrogen Energy. 2016 Jan;41(4):3199–207.

1072 10. Gogate MR. The direct dimethyl ether (DME) synthesis process from syngas I. Process feasibility
1073   and chemical synergy in one-step LPDME tm process. Pet Sci Technol. 2018 Apr 18;36(8):547–54.

1074 11. Edwards PP, Kuznetsov VL, David WIF, Brandon NP. Hydrogen and fuel cells: Towards a
1075   sustainable energy future. Energy Policy. 2008 Dec 1;36(12):4356–62.

1076 12. Hermesmann M, Müller TE. Green, Turquoise, Blue, or Grey? Environmentally friendly Hydrogen
1077   Production in Transforming Energy Systems. Prog Energy Combust Sci. 2022 May 1;90:100996.

1078 13. Yu M, Wang K, Vredenburg H. Insights into low-carbon hydrogen production methods: Green,
1079   blue and aqua hydrogen. Int J Hydrogen Energy. 2021 Jun;46(41):21261–73.

1080 14. Stiegel GJ, Ramezan M. Hydrogen from coal gasification: An economical pathway to a sustainable
1081   energy future. Int J Coal Geol. 2006 Jan;65(3–4):173–90.

1082 15. Azwar MY, Hussain MA, Abdul-Wahab AK. Development of biohydrogen production by
1083   photobiological, fermentation and electrochemical processes: A review. Renewable and
1084   Sustainable Energy Reviews. 2014 Mar 1;31:158–73.

1085 16. Lamb KE, Dolan MD, Kennedy DF. Ammonia for hydrogen storage; A review of catalytic ammonia
1086   decomposition and hydrogen separation and purification. Int J Hydrogen Energy. 2019 Feb
1087   5;44(7):3580–93.

1088 17. Yang J, Cui Z, Ma J, Dong Z. Ru coated Co nanoparticles decorated on cotton derived carbon
1089   fibers as a highly efficient and magnetically recyclable catalyst for hydrogen generation from
1090   ammonia borane. Int J Hydrogen Energy. 2018 Jan 18;43(3):1355–64.

1091 18. Holladay JD, Hu J, King DL, Wang Y. An overview of hydrogen production technologies. Catal
1092   Today. 2009 Jan 30;139(4):244–60.

1093 19. Steinfeld A. Solar thermochemical production of hydrogen—a review. Solar Energy. 2005 May
1094   1;78(5):603–15.

Energy Advances Accepted Manuscript

1095   20.   Gupta A, Likozar B, Jana R, Chanu WC, Singh MK. A review of hydrogen production processes by
1096   photocatalytic water splitting – From atomistic catalysis design to optimal reactor engineering.
1097   Int J Hydrogen Energy. 2022 Sep 12;47(78):33282–307.

1098   21.   Ji M, Wang J. Review and comparison of various hydrogen production methods based on costs
1099   and life cycle impact assessment indicators. Int J Hydrogen Energy. 2021 Nov;46(78):38612–35.

1100   22.   Ajanovic A, Sayer M, Haas R. The economics and the environmental benignity of different colors
1101   of hydrogen. Int J Hydrogen Energy. 2022 Jul 5;47(57):24136–54.

1102   23.   Santos DMF, Sequeira CAC, Figueiredo JL. Hydrogen production by alkaline water electrolysis.
1103   Quim Nova. 2013;36(8):1176–93.

1104   24.   Tee SY, Win KY, Teo WS, Koh L, Liu S, Teng CP, et al. Recent Progress in Energy-Driven Water
1105   Splitting. Advanced Science. 2017 May 13;4(5).

1106   25.   GRIGORIEV S, POREMBSKY V, FATEEV V. Pure hydrogen production by PEM electrolysis for
1107   hydrogen energy. Int J Hydrogen Energy. 2006 Feb;31(2):171–5.

1108   26.   Pettersson J, Ramsey B, Harrison D. A review of the latest developments in electrodes for
1109   unitised regenerative polymer electrolyte fuel cells. J Power Sources. 2006 Jun;157(1):28–34.

1110   27.   Hisatomi T, Kubota J, Domen K. Recent advances in semiconductors for photocatalytic and
1111   photoelectrochemical water splitting. Chem Soc Rev. 2014 Jan 13;43(22):7520–35.

1112   28.   Ali M, Pervaiz E, Noor T, Rabi O, Zahra R, Yang M. Recent advancements in <scp>MOF-</scp>
1113   based catalysts for applications in electrochemical and photoelectrochemical water splitting: A
1114   review. Int J Energy Res. 2021 Feb 24;45(2):1190–226.

1115   29.   Kudo A, Miseki Y. Heterogeneous photocatalyst materials for water splitting. Chem Soc Rev.
1116   2009;38(1):253–78.

1117   30.   Li X, Yu J, Low J, Fang Y, Xiao J, Chen X. Engineering heterogeneous semiconductors for solar
1118   water splitting. J Mater Chem A Mater. 2015;3(6):2485–534.

1119   31.   Zhao S, Zhang Y, Zhou Y, Fang J, Wang Y, Zhang C, et al. Fabrication of sandwich-structured g-
1120   C3N4/Au/BiOCl Z-scheme photocatalyst with enhanced photocatalytic performance under visible
1121   light irradiation. J Mater Sci. 2018 Apr 12;53(8):6008–20.

1122   32.   Xiao J, Han L, Luo J, Yu S, Jiang H. Integration of Plasmonic Effects and Schottky Junctions into
1123   Metal–Organic Framework Composites: Steering Charge Flow for Enhanced Visible-Light
1124   Photocatalysis. Angewandte Chemie International Edition. 2018 Jan 22;57(4):1103–7.

1125   33.   Wu Y, Wang P, Zhu X, Zhang Q, Wang Z, Liu Y, et al. Composite of $CH_3NH_3PbI_3$ with Reduced
1126   Graphene Oxide as a Highly Efficient and Stable Visible-Light Photocatalyst for Hydrogen
1127   Evolution in Aqueous HI Solution. Advanced Materials. 2018 Feb 8;30(7).

1128   34.   Wang X, Wang H, Zhang H, Yu W, Wang X, Zhao Y, et al. Dynamic Interaction between
1129   Methylammonium Lead Iodide and TiO_2 Nanocrystals Leads to Enhanced Photocatalytic H_2
1130   Evolution from HI Splitting. ACS Energy Lett. 2018 May 11;3(5):1159–64.

1131   35.   He K, Xie J, Yang Z, Shen R, Fang Y, Ma S, et al. Earth-abundant WC nanoparticles as an active
1132   noble-metal-free co-catalyst for the highly boosted photocatalytic H_2 production over g-C$_3$N$_4$
1133   nanosheets under visible light. Catal Sci Technol. 2017;7(5):1193–202.

1134   36.   Chen H, Jiang D, Sun Z, Irfan RM, Zhang L, Du P. Cobalt nitride as an efficient cocatalyst on CdS
1135   nanorods for enhanced photocatalytic hydrogen production in water. Catal Sci Technol.
1136   2017;7(7):1515–22.

1137   37.   Meng A, Zhang L, Cheng B, Yu J. Dual Cocatalysts in TiO$_2$ Photocatalysis. Advanced Materials.
1138   2019 Jul 30;31(30).

1139   38.   Ran J, Zhang J, Yu J, Jaroniec M, Qiao SZ. Earth-abundant cocatalysts for semiconductor-based
1140   photocatalytic water splitting. Chem Soc Rev. 2014;43(22):7787–812.

1141   39.   Knorr G, Hotzel K, Chettri A, Skabeev A, Wächtler M, Dietzek-Ivanšić B, et al. Unlocking the
1142   potential of ketocoumarins: efficient photosensitizers for sustainable light driven hydrogen
1143   evolution. J Mater Chem A Mater. 2023;11(43):23260–9.

1144   40.   Khalkhali FS, Kowsari E, Ramakrishna S, Eqbalpour M, Gheibi M, Esmaili H. A review on the
1145   photosensitizers used for enhancing the photoelectrochemical performance of hydrogen
1146   production with emphasis on a novel toxicity assessment framework. Int J Hydrogen Energy.
1147   2024 Jan;51:990–1022.

1148   41.   Leung CF, Lau TC. Organic Photosensitizers for Catalytic Solar Fuel Generation. Energy & Fuels.
1149   2021 Dec 2;35(23):18888–99.

1150   42.   Bassan E, Gualandi A, Cozzi PG, Ceroni P. Design of BODIPY dyes as triplet photosensitizers:
1151   electronic properties tailored for solar energy conversion, photoredox catalysis and
1152   photodynamic therapy. Chem Sci. 2021;12(19):6607–28.

1153   43.   Kim D, Dang VQ, Teets TS. Improved transition metal photosensitizers to drive advances in
1154   photocatalysis. Chem Sci. 2024;15(1):77–94.

1155   44.   Rana S, Kumar A, Dhiman P, Sharma G, Amirian J, Stadler FJ. Progress in graphdiyne and
1156   phosphorene based composites and heterostructures as new age materials for photocatalytic
1157   hydrogen evolution. Fuel. 2024 Jan 15;356:129630.

1158   45.   Li Q, Li X, Yu J. Surface and interface modification strategies of CdS-based photocatalysts.
1159   Interface Science and Technology. 2020 Jan 1;31:313–48.

1160   46.   Qiao S, Di M, Jiang JX, Han BH. Conjugated porous polymers for photocatalysis: The road from
1161   catalytic mechanism, molecular structure to advanced applications. EnergyChem. 2022 Nov
1162   1;4(6):100094.

1163   47.   Fox MA, Pettit TL. Photoactivity of zeolite-supported cadmium sulfide: hydrogen evolution in the
1164   presence of sacrificial donors. Langmuir. 1989 Jul 1;5(4):1056–61.

1165   48.   FUJISHIMA A, HONDA K. Electrochemical Photolysis of Water at a Semiconductor Electrode.
1166   Nature. 1972 Jul;238(5358):37–8.

Energy Advances Accepted Manuscript

1167   49.   Morales-Guio CG, Liardet L, Hu X. Oxidatively Electrodeposited Thin-Film Transition Metal
1168   (Oxy)hydroxides as Oxygen Evolution Catalysts. J Am Chem Soc. 2016 Jul 20;138(28):8946–57.

1169   50.   Xia X, Pan JH, Pan X, Hu L, Yao J, Ding Y, et al. Photochemical Conversion and Storage of Solar
1170   Energy. ACS Energy Lett. 2019 Feb 8;4(2):405–10.

1171   51.   Vayssieres L, Beermann N, Lindquist SE, Hagfeldt A. Controlled Aqueous Chemical Growth of
1172   Oriented Three-Dimensional Crystalline Nanorod Arrays: Application to Iron(III) Oxides.
1173   Chemistry of Materials. 2001 Feb 1;13(2):233–5.

1174   52.   Trotochaud L, Young SL, Ranney JK, Boettcher SW. Nickel–Iron Oxyhydroxide Oxygen-Evolution
1175   Electrocatalysts: The Role of Intentional and Incidental Iron Incorporation. J Am Chem Soc. 2014
1176   May 7;136(18):6744–53.

1177   53.   Paracchino A, Laporte V, Sivula K, Grätzel M, Thimsen E. Highly active oxide photocathode for
1178   photoelectrochemical water reduction. Nat Mater. 2011 Jun 8;10(6):456–61.

1179   54.   Bajaj R, Sharma M, Bahadur D. Visible light-driven novel nanocomposite (BiVO4/CuCr2O4) for
1180   efficient degradation of organic dye. Dalton Transactions. 2013;42(19):6736.

1181   55.   Frank SN, Bard AJ. Heterogeneous photocatalytic oxidation of cyanide ion in aqueous solutions at
1182   titanium dioxide powder. J Am Chem Soc. 1977 Jan 1;99(1):303–4.

1183   56.   Kalyanasundaram K. Applications of functionalized transition metal complexes in photonic and
1184   optoelectronic devices. Coord Chem Rev. 1998 Oct;177(1):347–414.

1185   57.   HODES G, CAHEN D, MANASSEN J. Tungsten trioxide as a photoanode for a photoelectrochemical
1186   cell (PEC). Nature. 1976 Mar;260(5549):312–3.

1187   58.   Kennedy JH, Frese KW. Photooxidation of Water at α - Fe2 O 3 Electrodes. J Electrochem Soc.
1188   1978 May 1;125(5):709–14.

1189   59.   Laursen AB, Kegnæs S, Dahl S, Chorkendorff I. Molybdenum sulfides—efficient and viable
1190   materials for electro - and photoelectrocatalytic hydrogen evolution. Energy Environ Sci.
1191   2012;5(2):5577.

1192   60.   Guerrero A, Bisquert J. Perovskite semiconductors for photoelectrochemical water splitting
1193   applications. Curr Opin Electrochem. 2017 Apr;2(1):144–7.

1194   61.   Darsan AS, Pandikumar A. Recent research progress on metal halide perovskite based visible light
1195   active photoanode for photoelectrochemical water splitting. Mater Sci Semicond Process. 2024
1196   May;174:108203.

1197   62.   Fan W, Lai Q, Zhang Q, Wang Y. Nanocomposites of TiO_2 and Reduced Graphene Oxide as
1198   Efficient Photocatalysts for Hydrogen Evolution. The Journal of Physical Chemistry C. 2011 Jun
1199   2;115(21):10694–701.

1200   63.   Marlinda AR, Yusoff N, Sagadevan S, Johan MR. Recent developments in reduced graphene oxide
1201   nanocomposites for photoelectrochemical water-splitting applications. Int J Hydrogen Energy.
1202   2020 Apr;45(21):11976–94.

1203   64.   Zhang YP, Tang HL, Dong H, Gao MY, Li CC, Sun XJ, et al. Covalent-organic framework based Z-
1204   scheme heterostructured noble-metal-free photocatalysts for visible-light-driven hydrogen
1205   evolution. J Mater Chem A Mater. 2020;8(8):4334–40.

1206   65.   Luan B, Chu X, Wang Y, Qiao X, Jiang Y, Zhang F. Construction of COF/COF Organic S-Scheme
1207   Heterostructure for Enhanced Overall Water Splitting. Advanced Materials. 2024 Dec 18;36(49).

1208   66.   Yu J, Sun X, Xu X, Zhang C, He X. Donor-acceptor type triazine-based conjugated porous polymer
1209   for visible-light-driven photocatalytic hydrogen evolution. Appl Catal B. 2019 Nov;257:117935.

1210   67.   Wong YL, Tobin JM, Xu Z, Vilela F. Conjugated porous polymers for photocatalytic applications. J
1211   Mater Chem A Mater. 2016;4(48):18677–86.

1212   68.   Bodedla GB, Imran M, Zhao J, Zhu X, Wong W. Design of AIEgen-based porphyrin for efficient
1213   heterogeneous photocatalytic hydrogen evolution. Aggregate. 2023 Oct 8;4(5).

1214   69.   Bodedla GB, Piradi V, Thor W, Wong KL, Zhu X, Wong WY. Self-assembly of Pt(<scp>ii</scp>)-
1215   tetrakis(pentafluorophenyl)porphyrin *via* F···F interaction for efficient cocatalyst-free
1216   photocatalytic hydrogen evolution. J Mater Chem A Mater. 2024;12(5):2924–31.

1217   70.   Bodedla GB, Piradi V, Imran M, Zhao J, Zhu X, Wong WY. Visible-to-near-infrared light-harvesting
1218   A-π-D-π-A porphyrins for boosted photocatalytic hydrogen evolution. J Mater Chem A Mater.
1219   2023;11(3):1473–81.

1220   71.   Abednatanzi S, Gohari Derakhshandeh P, Depauw H, Coudert FX, Vrielinck H, Van Der Voort P, et
1221   al. Mixed-metal metal–organic frameworks. Chem Soc Rev. 2019;48(9):2535–65.

1222   72.   Jiao L, Seow JYR, Skinner WS, Wang ZU, Jiang HL. Metal–organic frameworks: Structures and
1223   functional applications. Materials Today. 2019 Jul 1;27:43–68.

1224   73.   James SL. Metal-organic frameworks. Chem Soc Rev. 2003;32(5):276.

1225   74.   Schneemann A, Bon V, Schwedler I, Senkovska I, Kaskel S, Fischer RA. Flexible metal–organic
1226   frameworks. Chem Soc Rev. 2014 May 30;43(16):6062–96.

1227   75.   Pugh D, Ashworth E, Robertson K, Delmas LC, White AJP, Horton PN, et al. Metal–Organic
1228   Frameworks Constructed from Group 1 Metals (Li, Na) and Silicon-Centered Linkers. Cryst
1229   Growth Des. 2019 Jan 2;19(1):487–97.

1230   76.   Nguyen TLA, Demir-Cakan R, Devic T, Morcrette M, Ahnfeldt T, Auban-Senzier P, et al. 3-D
1231   Coordination Polymers Based on the Tetrathiafulvalenetetracarboxylate (TTF-TC) Derivative:
1232   Synthesis, Characterization, and Oxidation Issues. Inorg Chem. 2010 Aug 2;49(15):7135–43.

1233   77.   Deng H, Grunder S, Cordova KE, Valente C, Furukawa H, Hmadeh M, et al. Large-Pore Apertures
1234   in a Series of Metal-Organic Frameworks. Science (1979). 2012 May 25;336(6084):1018–23.

1235   78.   Benecke J, Svensson Grape E, Engesser TA, Inge AK, Reinsch H. Observation of three different
1236   linker conformers in a scandium ferrocenedicarboxylate coordination polymer. CrystEngComm.
1237   2020;22(34):5569–72.

1238 79. Banerjee D, Kim SJ, Parise JB. Lithium Based Metal–Organic Framework with Exceptional Stability.
1239   Cryst Growth Des. 2009 May 6;9(5):2500–3.

1240 80. Sun QZ, Yin YB, Chai LY, Liu H, Hao PF, Yan XP, et al. A novel 3D heterometallic coordination
1241   complex with (3,4,5)-connected net topology: Synthesis, structure and luminescent property. J
1242   Mol Struct. 2014 Jul;1070:75–9.

1243 81. Amombo Noa FM, Abrahamsson M, Ahlberg E, Cheung O, Göb CR, McKenzie CJ, et al. A unified
1244   topology approach to dot-, rod-, and sheet-MOFs. Chem. 2021 Sep;7(9):2491–512.

1245 82. Smolders S, Willhammar T, Krajnc A, Sentosun K, Wharmby MT, Lomachenko KA, et al. A
1246   Titanium(IV)-Based Metal–Organic Framework Featuring Defect-Rich Ti-O Sheets as an Oxidative
1247   Desulfurization Catalyst. Angewandte Chemie International Edition. 2019 Jul 27;58(27):9160–5.

1248 83. Peng Y, Huang H, Zhang Y, Kang C, Chen S, Song L, et al. A versatile MOF-based trap for heavy
1249   metal ion capture and dispersion. Nat Commun. 2018 Jan 15;9(1):187.

1250 84. Kamakura Y, Chinapang P, Masaoka S, Saeki A, Ogasawara K, Nishitani SR, et al. Semiconductive
1251   Nature of Lead-Based Metal–Organic Frameworks with Three-Dimensionally Extended Sulfur
1252   Secondary Building Units. J Am Chem Soc. 2020 Jan 8;142(1):27–32.

1253 85. Lee DW, Jo V, Ok KM. $Sr_2[C_6H_3(CO_2)_3(NO_3)]$·DMF: One-Dimensional Nano-Channel in a New
1254   Non-Centrosymmetric Strontium–Organic Framework with High Thermal Stability. Cryst Growth
1255   Des. 2011 Jul 6;11(7):2698–701.

1256 86. Fu Y, Su J, Zou Z, Yang S, Li G, Liao F, et al. Syntheses, Structures, and Gas Adsorption Properties
1257   of Two Novel Cadmium–Sodium Organic Frameworks with 1,3,5-Benzenetricarboxylate Ligands.
1258   Cryst Growth Des. 2011 Aug 3;11(8):3529–35.

1259 87. Behera D, Priyadarshini P, Parida K. ZIF-8 metal–organic frameworks and their hybrid materials:
1260   emerging photocatalysts for energy and environmental applications. Dalton Transactions. 2025;

1261 88. Chen B, Liang C, Yang J, Contreras DS, Clancy YL, Lobkovsky EB, et al. A Microporous Metal–
1262   Organic Framework for Gas-Chromatographic Separation of Alkanes. Angewandte Chemie
1263   International Edition. 2006 Feb 20;45(9):1390–3.

1264 89. Lee JY, Olson DH, Pan L, Emge TJ, Li J. Microporous Metal–Organic Frameworks with High Gas
1265   Sorption and Separation Capacity. Adv Funct Mater. 2007 May 21;17(8):1255–62.

1266 90. Pichon A, Lazuen-Garay A, James SL. Solvent-free synthesis of a microporous metal–organic
1267   framework. CrystEngComm. 2006;8(3):211.

1268 91. Férey G, Serre C, Mellot-Draznieks C, Millange F, Surblé S, Dutour J, et al. A Hybrid Solid with
1269   Giant Pores Prepared by a Combination of Targeted Chemistry, Simulation, and Powder
1270   Diffraction. Angewandte Chemie International Edition. 2004 Nov 26;43(46):6296–301.

1271 92. Wang B, Côté AP, Furukawa H, O'Keeffe M, Yaghi OM. Colossal cages in zeolitic imidazolate
1272   frameworks as selective carbon dioxide reservoirs. Nature. 2008 May;453(7192):207–11.

1273 93. Furukawa H, Ko N, Go YB, Aratani N, Choi SB, Choi E, et al. Ultrahigh Porosity in Metal-Organic
1274   Frameworks. Science (1979). 2010 Jul 23;329(5990):424–8.

1275 94.   Zheng ST, Bu JT, Li Y, Wu T, Zuo F, Feng P, et al. Pore Space Partition and Charge Separation in
1276   Cage-within-Cage Indium–Organic Frameworks with High CO_2 Uptake. J Am Chem Soc. 2010 Dec
1277   8;132(48):17062–4.

1278 95.   Zheng F, Xiang D, Li P, Zhang Z, Du C, Zhuang Z, et al. Highly Conductive Bimetallic Ni–Fe Metal
1279   Organic Framework as a Novel Electrocatalyst for Water Oxidation. ACS Sustain Chem Eng. 2019
1280   Jun 3;7(11):9743–9.

1281 96.   Huang L, Gao G, Zhang H, Chen J, Fang Y, Dong S. Self-dissociation-assembly of ultrathin metal-
1282   organic framework nanosheet arrays for efficient oxygen evolution. Nano Energy. 2020
1283   Feb;68:104296.

1284 97.   Elaouni A, El Ouardi M, Zbair M, BaQais A, Saadi M, Ait Ahsaine H. ZIF-8 metal organic framework
1285   materials as a superb platform for the removal and photocatalytic degradation of organic
1286   pollutants: a review. RSC Adv. 2022;12(49):31801–17.

1287 98.   Sadiq S, Khan I, Humayun M, Wu P, Khan A, Khan S, et al. Synthesis of Metal–Organic Framework-
1288   Based ZIF-8@ZIF-67 Nanocomposites for Antibiotic Decomposition and Antibacterial Activities.
1289   ACS Omega. 2023 Dec 26;8(51):49244–58.

1290 99.   Demir S, Çepni HM, Bilgin N, Hołyńska M, Yilmaz F. Metal–organic frameworks based on copper(I)
1291   iodide and pyridine-3,5-dicarboxylic acid: Synthesis, crystal structures and luminescent
1292   properties. Polyhedron. 2016 Sep;115:236–41.

1293 100. Ji H, Naveen K, Lee W, Kim TS, Kim D, Cho DH. Pyridinium-Functionalized Ionic Metal–Organic
1294   Frameworks Designed as Bifunctional Catalysts for CO_2 Fixation into Cyclic Carbonates. ACS Appl
1295   Mater Interfaces. 2020 Jun 3;12(22):24868–76.

1296 101. Luo G, Jiang J, Wei S, Huang C, Chen D, Zhu B, et al. Introducing sulfonic acid polymers into MOF
1297   nanochannels for ultra-high Ba2+ adsorption capacity and proton conductivity. Sep Purif Technol.
1298   2024 Sep;343:127133.

1299 102. Ghorbani-Vaghei R, Davood Azarifar DA, Daliran S, Oveisi AR. The UiO-66-SO_3H metal–organic
1300   framework as a green catalyst for the facile synthesis of dihydro-2-oxypyrrole derivatives. RSC
1301   Adv. 2016;6(35):29182–9.

1302 103. Enakieva YY, Sinelshchikova AA, Grigoriev MS, Chernyshev V V., Kovalenko KA, Stenina IA, et al.
1303   Highly Proton-Conductive Zinc Metal-Organic Framework Based On Nickel(II)
1304   Porphyrinylphosphonate. Chemistry – A European Journal. 2019 Aug 9;25(45):10552–6.

1305 104. Siemensmeyer K, Peeples CA, Tholen P, Schmitt F, Çoşut B, Hanna G, et al. Phosphonate Metal–
1306   Organic Frameworks: A Novel Family of Semiconductors. Advanced Materials. 2020 Jun 6;32(24).

1307 105. Li A, Yang X, Chen J. A novel route to size-controlled MIL-53(Fe) metal–organic frameworks for
1308   combined chemodynamic therapy and chemotherapy for cancer. RSC Adv. 2021;11(18):10540–7.

1309 106. Ahmadijokani F, Molavi H, Rezakazemi M, Tajahmadi S, Bahi A, Ko F, et al. UiO-66 metal–organic
1310   frameworks in water treatment: A critical review. Prog Mater Sci. 2022 Apr;125:100904.

Energy Advances Accepted Manuscript

1311   107.   Gordeeva LG, Solovyeva M V., Aristov YI. NH 2 -MIL-125 as a promising material for adsorptive
1312   heat transformation and storage. Energy. 2016 Apr;100:18–24.

1313   108.   Tranchemontagne DJ, Hunt JR, Yaghi OM. Room temperature synthesis of metal-organic
1314   frameworks: MOF-5, MOF-74, MOF-177, MOF-199, and IRMOF-0. Tetrahedron. 2008
1315   Sep;64(36):8553–7.

1316   109.   Lin KS, Adhikari AK, Ku CN, Chiang CL, Kuo H. Synthesis and characterization of porous HKUST-1
1317   metal organic frameworks for hydrogen storage. Int J Hydrogen Energy. 2012 Sep;37(18):13865–
1318   71.

1319   110.   Panda T, Pachfule P, Chen Y, Jiang J, Banerjee R. Amino functionalized zeolitic tetrazolate
1320   framework (ZTF) with high capacity for storage of carbon dioxide. Chem Commun.
1321   2011;47(7):2011–3.

1322   111.   Bonnett BL, Smith ED, De La Garza M, Cai M, Haag J V., Serrano JM, et al. PCN-222 Metal–Organic
1323   Framework Nanoparticles with Tunable Pore Size for Nanocomposite Reverse Osmosis
1324   Membranes. ACS Appl Mater Interfaces. 2020 Apr 1;12(13):15765–73.

1325   112.   Xie S, Qin Q, Liu H, Jin L, Wei X, Liu J, et al. MOF-74-M (M = Mn, Co, Ni, Zn, MnCo, MnNi, and
1326   MnZn) for Low-Temperature NH 3 -SCR and In Situ DRIFTS Study Reaction Mechanism. ACS Appl
1327   Mater Interfaces. 2020 Oct 28;12(43):48476–85.

1328   113.   Yuan S, Feng L, Wang K, Pang J, Bosch M, Lollar C, et al. Stable Metal–Organic Frameworks:
1329   Design, Synthesis, and Applications. Advanced Materials. 2018 Sep 12;30(37).

1330   114.   Eddaoudi M, Li H, Yaghi OM. Highly Porous and Stable Metal–Organic Frameworks: Structure
1331   Design and Sorption Properties. J Am Chem Soc. 2000 Feb 1;122(7):1391–7.

1332   115.   Li B, Wang H, Chen B. Microporous Metal–Organic Frameworks for Gas Separation. Chem Asian J.
1333   2014 Jun 25;9(6):1474–98.

1334   116.   Lin RB, Xiang S, Xing H, Zhou W, Chen B. Exploration of porous metal–organic frameworks for gas
1335   separation and purification. Coord Chem Rev. 2019 Jan 1;378:87–103.

1336   117.   Wang Z, Cohen SM. Postsynthetic modification of metal–organic frameworks. Chem Soc Rev.
1337   2009;38(5):1315.

1338   118.   Tanabe KK, Cohen SM. Postsynthetic modification of metal–organic frameworks—a progress
1339   report. Chem Soc Rev. 2011;40(2):498–519.

1340   119.   Rosi NL, Eddaoudi M, Kim J, O'Keeffe M, Yaghi OM. Advances in the chemistry of metal–organic
1341   frameworks. CrystEngComm. 2002;4(68):401–4.

1342   120.   Wu C, Zhao M. Incorporation of Molecular Catalysts in Metal–Organic Frameworks for Highly
1343   Efficient Heterogeneous Catalysis. Advanced Materials. 2017 Apr 3;29(14).

1344   121.   Yaghi OM, O'Keeffe M, Ockwig NW, Chae HK, Eddaoudi M, Kim J. Reticular synthesis and the
1345   design of new materials. Nature. 2003 Jun;423(6941):705–14.

1346   122.   Wang C, Liu X, Keser Demir N, Chen JP, Li K. Applications of water stable metal–organic
1347   frameworks. Chem Soc Rev. 2016;45(18):5107–34.

1348   123.   Kuppler RJ, Timmons DJ, Fang QR, Li JR, Makal TA, Young MD, et al. Potential applications of
1349   metal-organic frameworks. Coord Chem Rev. 2009 Dec 1;253(23–24):3042–66.

1350   124.   Farrusseng D, Aguado S, Pinel C. Metal–Organic Frameworks: Opportunities for Catalysis.
1351   Angewandte Chemie International Edition. 2009 Sep 28;48(41):7502–13.

1352   125.   Gong YN, Liu JW, Shao BZ, Zhong DC, Lu TB. Stable metal–organic frameworks for PEC water
1353   splitting. Vol. 27, FlatChem. Elsevier B.V.; 2021.

1354   126.   An Y, Liu Y, An P, Dong J, Xu B, Dai Y, et al. Ni ^{II} Coordination to an Al-Based Metal–Organic
1355   Framework Made from 2-Aminoterephthalate for Photocatalytic Overall Water Splitting.
1356   Angewandte Chemie International Edition. 2017 Mar 6;56(11):3036–40.

1357   127.   An Y, Xu B, Liu Y, Wang Z, Wang P, Dai Y, et al. Photocatalytic Overall Water Splitting over
1358   MIL-125(Ti) upon CoPi and Pt Co-catalyst Deposition. ChemistryOpen. 2017 Dec 7;6(6):701–5.

1359   128.   Remiro-Buenamañana S, Cabrero-Antonino M, Martínez-Guanter M, Álvaro M, Navalón S, García
1360   H. Influence of co-catalysts on the photocatalytic activity of MIL-125(Ti)-NH2 in the overall water
1361   splitting. Appl Catal B. 2019 Oct;254:677–84.

1362   129.   Cabrero-Antonino M, Albero J, García-Vallés C, Álvaro M, Navalón S, García H. Plasma-Induced
1363   Defects Enhance the Visible-Light Photocatalytic Activity of MIL-125(Ti)-NH$_2$ for Overall Water
1364   Splitting. Chemistry – A European Journal. 2020 Dec 18;26(67):15682–9.

1365   130.   Beltrán-Leiva MJ, Páez-Hernández D, Arratia-Pérez R. Theoretical Determination of Energy
1366   Transfer Processes and Influence of Symmetry in Lanthanide(III) Complexes: Methodological
1367   Considerations. Inorg Chem. 2018 May 7;57(9):5120–32.

1368   131.   Wang Y, Xu W, Lei L, Chen L, Ye R, Xu S. Photoluminescent NaGdF4@NaYF4:Ce/Tb inert-
1369   core/active-shell nanoparticles for selective and ultra-sensitive Cu2+ ions sensing. J Lumin. 2021
1370   Jul;235:118024.

1371   132.   Kuang Y, Xu J, Wang C, Li T, Gai S, He F, et al. Fine-Tuning Ho-Based Red-Upconversion
1372   Luminescence by Altering NaHoF$_4$ Core Size and NaYbF$_4$ Shell Thickness. Chemistry of Materials.
1373   2019 Oct 8;31(19):7898–909.

1374   133.   Zhao S, Li L, Song X, Zhu M, Hao Z, Meng X, et al. Lanthanide Ion Codoped Emitters for Tailoring
1375   Emission Trajectory and Temperature Sensing. Adv Funct Mater. 2015 Mar 27;25(9):1463–9.

1376   134.   Song Y, Pi Y, Feng X, Ni K, Xu Z, Chen JS, et al. Cerium-Based Metal–Organic Layers Catalyze
1377   Hydrogen Evolution Reaction through Dual Photoexcitation. J Am Chem Soc. 2020 Apr
1378   15;142(15):6866–71.

1379   135.   Reddy ChV, Reddy KR, Harish VVN, Shim J, Shankar MV, Shetti NP, et al. Metal-organic
1380   frameworks (MOFs)-based efficient heterogeneous photocatalysts: Synthesis, properties and its
1381   applications in photocatalytic hydrogen generation, CO2 reduction and photodegradation of
1382   organic dyes. Int J Hydrogen Energy. 2020 Mar;45(13):7656–79.

1383 136. Liu S, Zhang C, Sun Y, Chen Q, He L, Zhang K, et al. Design of metal-organic framework-based
1384   photocatalysts for hydrogen generation. Coord Chem Rev. 2020 Jun;413:213266.

1385 137. Luo H, Zeng Z, Zeng G, Zhang C, Xiao R, Huang D, et al. Recent progress on metal-organic
1386   frameworks based- and derived-photocatalysts for water splitting. Chemical Engineering Journal.
1387   2020 Mar;383:123196.

1388 138. Nguyen HL. Metal–Organic Frameworks for Photocatalytic Water Splitting. Solar RRL. 2021 Jul
1389   20;5(7).

1390 139. Xiao Y, Guo X, Yang N, Zhang F. Heterostructured MOFs photocatalysts for water splitting to
1391   produce hydrogen. Journal of Energy Chemistry. 2021 Jul;58:508–22.

1392 140. Sun X, Yuan K, Zhang Y. Advances and prospects of rare earth metal-organic frameworks in
1393   catalytic applications. Journal of Rare Earths. 2020 Aug;38(8):801–18.

1394 141. Sun K, Qian Y, Jiang H. Metal-Organic Frameworks for Photocatalytic Water Splitting and CO$_2$
1395   Reduction. Angewandte Chemie. 2023 Apr 3;135(15).

1396 142. Nordin NA, Mohamed MA, Salehmin MNI, Mohd Yusoff SF. Photocatalytic active metal–organic
1397   framework and its derivatives for solar-driven environmental remediation and renewable energy.
1398   Coord Chem Rev. 2022 Oct;468:214639.

1399 143. Saraci F, Quezada-Novoa V, Donnarumma PR, Howarth AJ. Rare-earth metal–organic
1400   frameworks: from structure to applications. Chem Soc Rev. 2020;49(22):7949–77.

1401 144. Shi X, Cao B, Liu J, Zhang J, Du Y. Rare-Earth-Based Metal–Organic Frameworks as Multifunctional
1402   Platforms for Catalytic Conversion. Vol. 17, Small. John Wiley and Sons Inc; 2021.

1403 145. Fan C, Dong W, Saira Y, Tang Y, Fu G, Lee J. Rare-Earth–Modified Metal–Organic Frameworks and
1404   Derivatives for Photo/Electrocatalysis. Small. 2023 Oct 8;19(41).

1405 146. Meng S, Li G, Wang P, He M, Sun X, Li Z. Rare earth-based MOFs for photo/electrocatalysis. Mater
1406   Chem Front. 2023;7(5):806–27.

1407 147. Zhang Y, Wei P, Li Z, Sun Y, Liu Y, Huang S. Advancements in rare earth metal-organic
1408   frameworks: Harnessing the power of photonics and beyond. Coord Chem Rev. 2024
1409   Sep;514:215905.

1410 148. Zhang Y, Liu S, Zhao ZS, Wang Z, Zhang R, Liu L, et al. Recent progress in lanthanide metal-organic
1411   frameworks and their derivatives in catalytic applications. Vol. 8, Inorganic Chemistry Frontiers.
1412   Royal Society of Chemistry; 2021. p. 590–619.

1413 149. News from Catalysis Science & Technology. Catal Sci Technol. 2016;6(11):3647–8.

1414 150. Editorial Board. J Catal. 2022 Jan;405:ii.

1415 151. Zhou HC "Joe", Kitagawa S. Metal–Organic Frameworks (MOFs). Chem Soc Rev. 2014 Jul
1416   10;43(16):5415–8.

Energy Advances Accepted Manuscript

1417   152.   Cheng JW, Zheng ST, Yang GY. Diversity of crystal structure with different lanthanide ions
1418   involving in situ oxidation–hydrolysis reaction. Dalton Transactions. 2007;(36):4059.

1419   153.   Chen B, Yang Y, Zapata F, Lin G, Qian G, Lobkovsky EB. Luminescent Open Metal Sites within a
1420   Metal–Organic Framework for Sensing Small Molecules. Advanced Materials. 2007 Jul
1421   2;19(13):1693–6.

1422   154.   Ramya AR, Sharma D, Natarajan S, Reddy MLP. Highly Luminescent and Thermally Stable
1423   Lanthanide Coordination Polymers Designed from 4-(Dipyridin-2-yl)aminobenzoate: Efficient
1424   Energy Transfer from Tb^{3+} to Eu^{3+} in a Mixed Lanthanide Coordination Compound. Inorg Chem.
1425   2012 Aug 20;51(16):8818–26.

1426   155.   Zhang T, Lin W. Metal–organic frameworks for artificial photosynthesis and photocatalysis. Chem
1427   Soc Rev. 2014;43(16):5982–93.

1428   156.   Batubara NH, Zulys A. Synthesis, Structural, Spectroscopic, and Morphology of Metal-Organic
1429   Frameworks Based on La (III) and Ligand 2,6-Napthalenedicarboxylic acid (La-MOFs) for Hydrogen
1430   Production. IOP Conf Ser Mater Sci Eng. 2019 Jun 1;546(4):042005.

1431   157.   Melillo A, Cabrero-Antonino M, Navalón S, Álvaro M, Ferrer B, García H. Enhancing visible-light
1432   photocatalytic activity for overall water splitting in UiO-66 by controlling metal node
1433   composition. Appl Catal B. 2020 Dec;278:119345.

1434   158.   Allendorf MD, Bauer CA, Bhakta RK, Houk RJT. Luminescent metal–organic frameworks. Chem
1435   Soc Rev. 2009;38(5):1330.

1436   159.   Zhou JM, Shi W, Xu N, Cheng P. Highly Selective Luminescent Sensing of Fluoride and Organic
1437   Small-Molecule Pollutants Based on Novel Lanthanide Metal–Organic Frameworks. Inorg Chem.
1438   2013 Jul 15;52(14):8082–90.

1439   160.   Yang QY, Li K, Luo J, Pan M, Su CY. A simple topological identification method for highly (3,12)-
1440   connected 3D MOFs showing anion exchange and luminescent properties. Chemical
1441   Communications. 2011;47(14):4234.

1442   161.   Hao JN, Yan B. Ag^+-sensitized lanthanide luminescence in Ln^{3+} post-functionalized metal–
1443   organic frameworks and Ag^+ sensing. J Mater Chem A Mater. 2015;3(9):4788–92.

1444   162.   Sun D, Liu W, Qiu M, Zhang Y, Li Z. Introduction of a mediator for enhancing photocatalytic
1445   performance via post-synthetic metal exchange in metal–organic frameworks (MOFs). Chemical
1446   Communications. 2015;51(11):2056–9.

1447   163.   Santiago Portillo A, Baldoví HG, García Fernandez MT, Navalón S, Atienzar P, Ferrer B, et al. Ti as
1448   Mediator in the Photoinduced Electron Transfer of Mixed-Metal NH_2–UiO-66(Zr/Ti): Transient
1449   Absorption Spectroscopy Study and Application in Photovoltaic Cell. The Journal of Physical
1450   Chemistry C. 2017 Mar 30;121(12):7015–24.

1451   164.   Liu W, Zhang S, Wu B, Gong X, Shao J, Wang S, et al. Platinum-Assisted Bimetallic Ru–Eu/Pr MOFs
1452   for Photocatalytic H_2 Evolution from Water Splitting. ACS Appl Nano Mater. 2023 Sep
1453   22;6(18):16826–36.

Energy Advances Accepted Manuscript

1454 165. Gu J, Zhao P, Lin W, Deng J, Chao Z, Jin H. Cerium (III)-MOF as a photocatalyst for hydrogen
1455   evolution from water splitting. Appl Organomet Chem. 2024 Jul 4;

1456 166. Mahata P, Mondal SK, Singha DK, Majee P. Luminescent rare-earth-based MOFs as optical
1457   sensors. Dalton Transactions. 2017;46(2):301–28.

1458 167. Wang F, Pu Y, Zhang X, Zhang F, Cheng H, Zhao Y. A series of multifunctional lanthanide metal-
1459   organic frameworks for luminescent sensing and photocatalytic applications. J Lumin. 2019
1460   Feb;206:192–8.

1461 168. An Y, Liu Y, Bian H, Wang Z, Wang P, Zheng Z, et al. Improving the photocatalytic hydrogen
1462   evolution of UiO-67 by incorporating Ce4+-coordinated bipyridinedicarboxylate ligands. Sci Bull
1463   (Beijing). 2019 Oct;64(20):1502–9.

1464 169. Yang H, Jia L, Zhang Z, Xu B, Liu Z, Zhang Q, et al. Novel cerium-based MOFs photocatalyst for
1465   photocarrier collaborative performance under visible light. J Catal. 2022 Jan;405:74–83.

1466 170. He J, Wang J, Chen Y, Zhang J, Duan D, Wang Y, et al. A dye-sensitized Pt@UiO-66(Zr) metal–
1467   organic framework for visible-light photocatalytic hydrogen production. Chem Commun.
1468   2014;50(53):7063–6.

1469 171. Wang C, Xie Z, deKrafft KE, Lin W. Doping Metal–Organic Frameworks for Water Oxidation,
1470   Carbon Dioxide Reduction, and Organic Photocatalysis. J Am Chem Soc. 2011 Aug
1471   31;133(34):13445–54.

1472 172. Toyao T, Saito M, Dohshi S, Mochizuki K, Iwata M, Higashimura H, et al. Development of a Ru
1473   complex-incorporated MOF photocatalyst for hydrogen production under visible-light irradiation.
1474   Chemical Communications. 2014;50(51):6779.

1475 173. Hou CC, Li TT, Cao S, Chen Y, Fu WF. Incorporation of a [Ru(dcbpy)(bpy)$_2$]$^{2+}$ photosensitizer and
1476   a Pt(dcbpy)Cl$_2$ catalyst into metal–organic frameworks for photocatalytic hydrogen evolution
1477   from aqueous solution. J Mater Chem A Mater. 2015;3(19):10386–94.

1478 174. Feng Y, Chen C, Liu Z, Fei B, Lin P, Li Q, et al. Application of a Ni mercaptopyrimidine MOF as
1479   highly efficient catalyst for sunlight-driven hydrogen generation. J Mater Chem A Mater.
1480   2015;3(13):7163–9.

1481 175. Sun X, Yu Q, Zhang F, Wei J, Yang P. A dye-like ligand-based metal–organic framework for
1482   efficient photocatalytic hydrogen production from aqueous solution. Catal Sci Technol.
1483   2016;6(11):3840–4.

1484 176. Yu Q, Dong H, Zhang X, Zhu YX, Wang JH, Zhang FM, et al. Novel stable metal–organic framework
1485   photocatalyst for light-driven hydrogen production. CrystEngComm. 2018;20(23):3228–33.

1486 177. Zhao S, Liang Q, Gao W, Zhou M, Yao C, Xu S, et al. *In Situ* Growth of ZnIn$_2$S$_4$ on MOF-Derived
1487   Ni–Fe LDH to Construct Ternary-Shelled Nanotubes for Efficient Photocatalytic Hydrogen
1488   Evolution. Inorg Chem. 2021 Jul 5;60(13):9762–72.

1489   178.   Li Z, Wang X, Tian W, Meng A, Yang L. CoNi Bimetal Cocatalyst Modifying a Hierarchical $ZnIn_2S_4$
1490   Nanosheet-Based Microsphere Noble-Metal-Free Photocatalyst for Efficient Visible-Light-Driven
1491   Photocatalytic Hydrogen Production. ACS Sustain Chem Eng. 2019 Dec 16;7(24):20190–201.

1492   179.   Liu J, Chen G, Sun J. Ag_2S-Modified $ZnIn_2S_4$ Nanosheets for Photocatalytic H_2 Generation. ACS
1493   Appl Nano Mater. 2020 Nov 25;3(11):11017–24.

1494   180.   Li Q, Xia Y, Yang C, Lv K, Lei M, Li M. Building a direct Z-scheme heterojunction photocatalyst by
1495   ZnIn2S4 nanosheets and TiO2 hollowspheres for highly-efficient artificial photosynthesis.
1496   Chemical Engineering Journal. 2018 Oct;349:287–96.

1497   181.   Kong D, Fan H, Yin D, Zhang D, Pu X, Yao S, et al. $AgFeO_2$ Nanoparticle/$ZnIn_2S_4$ Microsphere p–n
1498   Heterojunctions with Hierarchical Nanostructures for Efficient Visible-Light-Driven H_2 Evolution.
1499   ACS Sustain Chem Eng. 2021 Feb 22;9(7):2673–83.

1500   182.   Yuan YJ, Chen D, Zhong J, Yang LX, Wang J, Liu MJ, et al. Interface engineering of a noble-metal-
1501   free 2D–2D MoS_2/Cu-$ZnIn_2S_4$ photocatalyst for enhanced photocatalytic H_2 production. J
1502   Mater Chem A Mater. 2017;5(30):15771–9.

1503   183.   Sowik J, Grzyb T, Trykowski G, Klimczuk T, Nikiforow K, Cavdar O, et al. Lanthanide-organic-
1504   frameworks modified ZnIn2S4 for boosting hydrogen generation under UV–Vis and visible light.
1505   Int J Hydrogen Energy. 2022 Apr 29;47(36):16065–79.

1506   184.   Kundu J, Mal DD, Pradhan D. Single-step solvothermal synthesis of highly uniform $Cd_xZn_{1-x}S$
1507   nanospheres for improved visible light photocatalytic hydrogen generation. Inorg Chem Front.
1508   2021;8(12):3055–65.

1509   185.   Li TT, Chen Y, Cheng Y, Zheng MQ, Qian JF, He MY, et al. Synthesis of rare earth MOF/CZS
1510   materials derived from aromatic tetracarboxylic acids and photocatalytic hydrogen production.
1511   Int J Hydrogen Energy. 2024 May 2;65:225–35.

1512   186.   Zhang L, Jin Z, Huang S, Zhang Y, Zhang M, Zeng YJ, et al. Ce-Doped Graphitic Carbon Nitride
1513   Derived from Metal Organic Frameworks as a Visible Light-Responsive Photocatalyst for H2
1514   Production. Nanomaterials. 2019 Oct 30;9(11):1539.

1515   187.   Hao J, Zhan W, Sun L, Zhuang G, Wang X, Han X. Combining N,S-Codoped C and CeO_2: A Unique
1516   Hinge-like Structure for Efficient Photocatalytic Hydrogen Evolution. Inorg Chem. 2020 Jan
1517   6;59(1):937–42.

1518   188.   Wu P, Guo X, Cheng L, He C, Wang J, Duan C. Photoactive Metal-Organic Framework and Its Film
1519   for Light-Driven Hydrogen Production and Carbon Dioxide Reduction. Inorg Chem. 2016 Aug
1520   15;55(16):8153–9.

1521   189.   Anderson SL, Tiana D, Ireland CP, Capano G, Fumanal M, Gładysiak A, et al. Taking lanthanides
1522   out of isolation: tuning the optical properties of metal–organic frameworks. Chem Sci.
1523   2020;11(16):4164–70.

1524   190.   Hidalgo-Rosa Y, Saavedra-Torres M, Koivisto BD, Treto-Suárez MA, Páez-Hernández D, Zarate X,
1525   et al. Rare-earth-based metal–organic frameworks with improved visible-light-harvesting
1526   properties: a quantum chemistry study. J Mater Sci. 2023 Jun 25;58(21):8862–77.

Energy Advances Accepted Manuscript

1527 191. Mahata P, Ramya KV, Natarajan S. Pillaring of CdCl$_2$ -Like Layers in Lanthanide Metal–Organic
1528   Frameworks: Synthesis, Structure, and Photophysical Properties. Chemistry – A European
1529   Journal. 2008 Jun 27;14(19):5839–50.

1530 192. Mahata P, Ramya K V., Natarajan S. Synthesis, structure and optical properties of rare-earth
1531   benzene carboxylates. Dalton Transactions. 2007;(36):4017.

1532 193. Yang J, Yue Q, Li GD, Cao JJ, Li GH, Chen JS. Structures, Photoluminescence, Up-Conversion, and
1533   Magnetism of 2D and 3D Rare-Earth Coordination Polymers with Multicarboxylate Linkages.
1534   Inorg Chem. 2006 Apr 1;45(7):2857–65.

1535

Data Availability Statement

Data sharing is not applicable to this review article as no new data were created or analyzed in this study.

Authors: P. Danita Patricia and Dr. Rajadurai Vijay Solomon